Research Square

Preprints are preliminary reports that have not undergone peer review.
They should not be considered conclusive, used to inform clinical practice,
or referenced by the media as validated information.

An Asymmetric Quasi-zero Stiffness Vibration Isolator with Long Stroke and Large Bearing Capacity

Xinghua Zhou
Jilin University
Dingxuan Zhao (zdx-yw@ysu.edu.cn)
Yanshan University
Xiao Sun
Jilin University
Xiao Yang
Jilin University
Jianhai Zhang
Jilin University
Tao Ni
Yanshan University
Kehong Tang
Jilin University

Research Article

Keywords: Passive vibration isolator, Asymmetric quasi-zero stiffness, Nonlinear stiffness, Cantilever plate spring, L-shaped lever.

Posted Date: July 30th, 2021

DOI: https://doi.org/10.21203/rs.3.rs-730417/v1

License: This work is licensed under a Creative Commons Attribution 4.0 International License.
Read Full License

Version of Record: A version of this preprint was published at Nonlinear Dynamics on March 15th, 2022.
See the published version at https://doi.org/10.1007/s11071-022-07300-1.

An asymmetric quasi-zero stiffness vibration isolator with long stroke and large bearing capacity

Xinghua Zhou [a], Dingxuan Zhao [b, *], Xiao Sun [a], Xiao Yang [a], Jianhai Zhang [a], Tao Ni [b], Kehong Tang [a]

[a] School of Mechanical and Aerospace Engineering, Jilin University, Changchun 130022, China

[b] School of Mechanical Engineering, Yanshan University, Qinhuangdao 066004, China

[*] Corresponding author: Dingxuan Zhao (zdx-yw@ysu.edu.cn)

Abstract

A novel passive asymmetric quasi-zero stiffness vibration isolator (AQZS-VI) comprising two linear springs acting in parallel with one negative stiffness element (NSE) is proposed, of which the NSE is mainly constructed by the combination of cantilever plate spring and L-shaped lever (CPS-LSL). The static model of the isolator is deduced considering the geometrical nonlinearity of the NSE and the bending deformation of plate spring. The nonlinear stiffness properties of the CPS-LSL and the AQZS-VI, as well as the nonlinear damping properties of the AQZS-VI are discussed. The absolute displacement transmissibility of the AQZS-VI under base displacement excitation is obtained using Harmonic Balance Method, and the effects of different excitation amplitudes and damping factors on the vibration isolation performance are analyzed. Better than other quasi-zero stiffness vibration isolators (QZS-VI) whose NSEs do not provide supporting force at zero stiffness point, the NSE of the AQZS-VI provides more supporting force than the parallel connected linear springs, which is very beneficial for improving the bearing capacity of the isolator. Compared with a typical symmetric QZS-VI with same damping property, the AQZS-VI has longer stroke with

low stiffness and lower peak value of displacement transmissibility. The prototype experiments indicate that the AQZS-VI outperforms the linear counterpart with much smaller starting frequency of vibration isolation and lower displacement transmissibility. The proposed AQZS-VI has great potential for applying in various engineering practices with superior vibration isolation performance.

Keywords: Passive vibration isolator; Asymmetric quasi-zero stiffness; Nonlinear stiffness; Cantilever plate spring; L-shaped lever.

1. Introduction

Mechanical vibration is undesirable in most engineering practice. It affects the mechanical properties, aggravates wear and fatigue, and even causes structural damage. Installment of vibration isolators between vibration source and isolated objects is a common way for vibration isolation and has been widely used to maintain the reliable operation of precision instruments [1, 2], improve the comfort of vehicle ride [3-5], assist space launch or on-orbit operation [6], ensure the safety of building constructions or bridge structures [7, 8] and so on. With the development of vibration isolation technology, diverse vibration isolators have emerged to cope with the ever increasing demands for high vibration isolation performance, especially the demands for low frequency and even ultra-low frequency vibration isolation [9, 10]. Nonlinear passive vibration isolators, possessing high static and low dynamic stiffness (HSLDS) and nonlinear damping properties, are suitable for low or ultra-low frequency isolation. The high static and low dynamic stiffness provide the nonlinear isolators with large bearing capacity (requiring high static stiffness) and low starting frequency of vibration isolation (requiring low dynamic stiffness) under limited spring preload. And the nonlinear damping properties give the chance for the nonlinear isolators to obtain low vibration transmissibility both at resonant frequency and higher frequencies [11].

As typical nonlinear passive HSLDS vibration isolators, passive quasi-zero stiffness vibration isolators (QZS-VI) have drawn much attentions of engineers and researchers for the superior vibration isolation performance as mentioned above. The common way to construct the passive QZS-VI is parallel connecting negative stiffness element (NSE) with positive stiffness mechanism. According to the composition and structures of NSEs (e.g., oblique spring, horizontal spring, cam-roller-spring, magnetic spring, Euler buckled beam), diverse types of passive QZS-VIs can be constructed [3, 5, 12-22]. Waters and his co-workers [12, 13] studied the static and dynamic characteristic of QZS-VI with two oblique springs served as NSE. Le et al. [3] and Hu et al. [14] presented the isolation system, in which horizontal springs are hinged with rigid rods to provide negative stiffness. The isolation system can create large frequency band of isolation and exhibit excellent isolation performance. Zhou et al. [15] and Liu et al. [16] developed the QZS-VIs equipped with cam-roller-spring mechanisms, and the results verified that the QZS-VIs outperform the linear counterparts with lower initial isolation frequency and better isolation performance around resonant frequency. Professor Hua and his colleagues [18, 21] conducted the theoretical and experimental studies on the QZS-VI, in which the axial motion of the Euler buckled beams provide negative stiffness force (NSF). By introducing the NSF, the starting frequency of isolation of the QZS-VI is lower than that of the linear isolator with the same supporting capacity. A series of researches reveal that the passive QZS-VIs can produce lower starting frequency of vibration isolation and smaller displacement/force transmissibility than the linear counterparts. While the stiffness of most QZS-VIs mentioned above are symmetrical about zero stiffness point (ZSP) or static equilibrium position (SEP), of which the negative stiffness elements have no contribution to the bearing capacity of QZS-VIs at ZSP/SEP. And the range of displacement near the ZSP/SEP is relatively small when the stiffness is less than a prescribed low value.

The nonlinear passive vibration isolators constructed by single nonlinear

geometrical elements are another type of isolators, which exhibit asymmetric stiffness properties and superior vibration isolation performance. Professor Jing and his team [23-29] proposed scissor-like truss structured vibration isolators with equivalent nonlinear stiffness and damping characteristics. The scissor-like structured isolators possessing inherent geometrical nonlinearities have lower starting frequency of isolation than linear isolators and are more stable than QZS-VIs. While, for the single nonlinear geometrical vibration isolators, it is not easy to realize ultra-low frequency vibration isolation for that its dynamic stiffness is hard to approach zero.

An asymmetric quasi-zero stiffness vibration isolator (AQZS-VI) constructed by single nonlinear geometrical vibration isolator and positive stiffness springs is expected to obtain excellent vibration isolation performance with large bearing capacity, low stiffness in wide displacement range, i.e., long stroke, and ultra-low frequency isolation. Yan et al. [30] proposed a long stroke QZS-VI which is constructed by parallel connection of the symmetric polygon structure and linear springs. Research results demonstrate that the long stroke QZS-VI has a lower resonant frequency, outperforms the linear counterpart especially at low frequencies, and is less sensitive to vibration amplitude than the traditional QZS-VI. Recently, we designed and analyzed a passive AQZS-VI with the combination of plate spring and V-shaped levers served as NSE [31]. The theoretical analysis results showed that the AQZS-VI has superior vibration isolation performance and great potential for engineering applications. What's missing is that the dynamic analysis of the nonlinear isolator in our previous research [31] is based on the third Taylor series expansion of restoring force, of which the expansion curve can’t well fit the analytical curve of restoring force along large displacement range. In addition, the internal friction of each kinematic pair in the vibration isolator is simplified as linear viscous friction, and the intrinsic nonlinear friction damping characteristics such as Coulomb friction is neglected. Most importantly, the results obtained from theoretical analysis are not verified by prototype experiments.

For further investigation, we developed a novel passive AQZS-VI whose structure is more suitable for engineering application. Specifically, a NSE mainly comprised of the combination of cantilever plate spring and L-shaped lever (CPS-LSL) was constructed and then connected in parallel with two linear springs. The non-dimensional static model which concerns the geometrical nonlinearity of the NSE and the bending deformation of plate spring was derived. Considering the Coulomb friction of each kinematic pair, the nonlinear damping characteristic of the vibration isolator was analyzed. The isolation performance of the AQZS-VI under base displacement excitation was discussed. Comparisons with linear vibration isolator and typical symmetric QZS-VI were also conducted to evaluate the excellent vibration isolation performance of proposed AQZS-VI. To verify the accuracy of the static model and the superior vibration isolation performance of AQZS-VI, the prototype was manufactured and series of static and dynamic experiments were conducted.

The rest of this paper is organized as follows. The AQZS-VI equipped with CPS-LSL is introduced in Section 2 and the mathematical model of AQZS-VI is established in Section 3. The non-dimensional stiffness of both CPS-LSL and the vibration isolator, as well as the damping properties of the vibration isolator are analyzed in Section 4. The absolute displacement transmissibility under different amplitudes of excitation and damping factors are studied in Section 5. The vibration isolation performance of the AQZS-VI is compared with that of typical symmetric QZS-VI and of linear vibration isolator in Section 6. The experimental investigation is presented in Section 7, followed by the conclusions and discussions.

2. The AQZS-VI equipped with CPS-LSL

The AQZS-VI is mainly comprised of one CPS-LSL and two vertical coil springs, as shown in **Fig. 1**. The CPS-LSL served as NSE is mainly constructed by one plate spring, two L-shaped levers and two horizontal guiding combinations. The center part

of plate spring is fixed on the vertical plate of the base, and both ends are in cantilever state. Two L-shaped levers are symmetrically installed between the supporting platform and the base. Specifically, the long arm end of each L-shaped lever is hinged with the bottom supporting rod of the platform. The short arm end of each L-shaped lever contacts with the plate spring and can slide on the surface of the plate spring. The elbow joints of two L-shaped levers are hinged on two horizontal guiding components, which can slide on two horizontal guiding shafts. The left and right ends of the two horizontal guiding shafts are parallel installed on two supporting plates of the base. Two vertical guiding components are mounted between the platform and the base to ensure that the platform moves along the vertical direction. Two linear coil springs and the CPS-LSL are connected in parallel to offset negative dynamic stiffness of the CPS-LSL, so as to making the nonlinear isolator achieving high static and low dynamic stiffness.

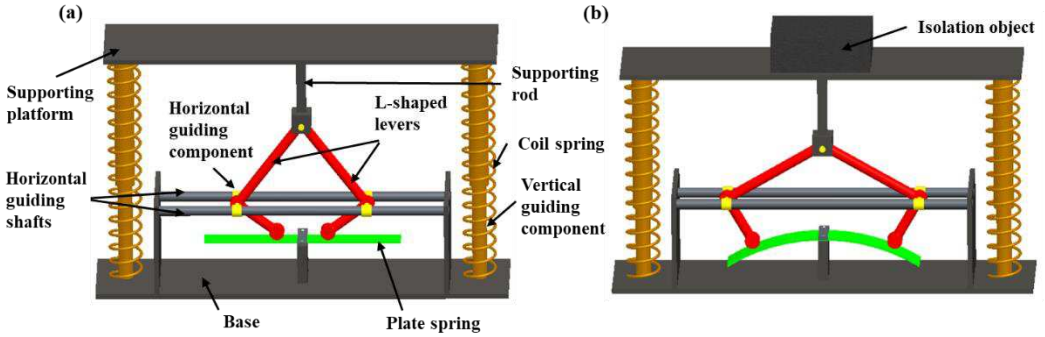


Fig. 1 Physical model of the AQZS-VI: (a) without load; (b) with load.

In initial state, no payload acts on the platform and the plate spring remains un-deformed, as shown in **Fig. 1a**. After loading the isolation object, two coil springs are compressed, and two L-shaped levers rotate around two horizontal guiding components. At the same time, two horizontal guiding components slide away from each other along two horizontal guiding shafts, forcing the plate spring to bend, as shown in **Fig. 1b**. With the increase of plate spring bending, the negative dynamic stiffness of CPS-LSL occurs. By connecting two positive stiffness springs in parallel with CPS-LSL, the

quasi-zero stiffness properties of the nonlinear isolator can be obtained.

The schematic of the AQZS-VI, with clear designation of the structural parameters, is shown in **Fig. 2**. The short and long arms of each L-shaped lever are perpendicular to each other, whose lengths are marked as l_1 and l_2, respectively. The vertical distance from the fixed end of cantilever plate spring to the horizontal guiding shaft is denoted by *d*. The stiffness of each coil spring is k/2. The mass of the isolation object is m. The absolute movement of the isolation object is denoted by *x*, the base excitation is *z*, both of their positive directions are defined as vertical down.

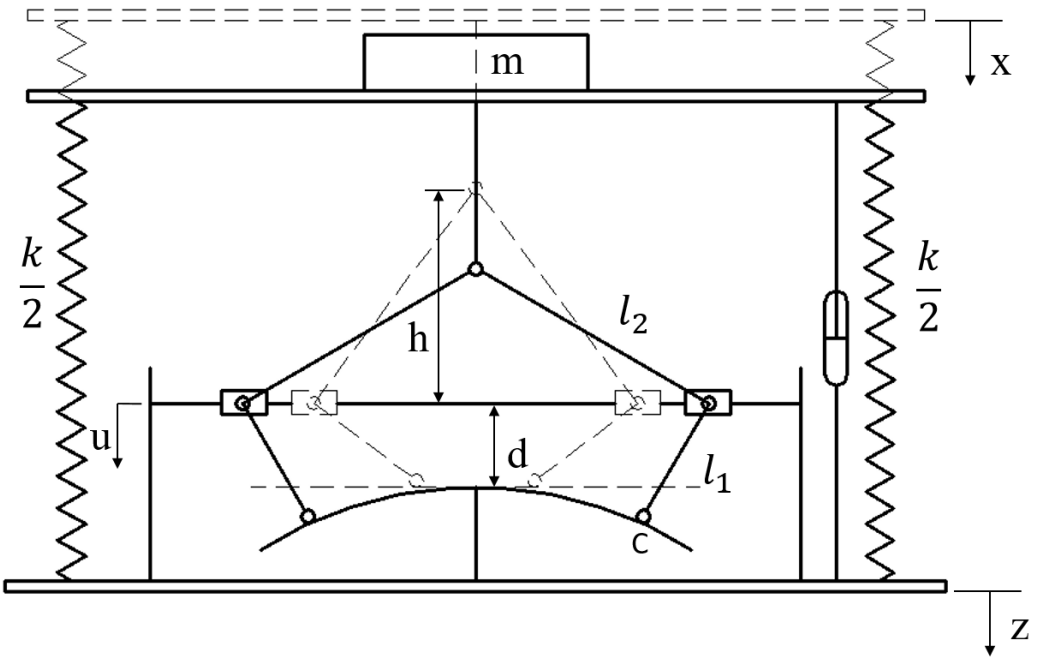


Fig. 2 Schematic diagram of the AQZS-VI.

3. Modeling of the AQZS-VI

3.1 Static model

As seen in **Fig. 1**, the structure of AQZS-VI is symmetrical about the axis of the vertical supporting rod. To clearly reveal the relationship between the restoring force and the deformation of AQZS-VI along vertical direction, the force and deformation

diagrams of one L-shaped lever and half of plate spring are depicted in **Fig. 3 (a) and (b) respectively**. The coordinate system *Ovw* is defined, of which the origin (*O*) is set on the center of the plate spring, and the positive directions of horizontal (*v*) and vertical (*w*) axes are defined as right and down, respectively. The inclination angle of the long arm of L-shaped lever relative to the vertical direction is α. The coordinate of endpoint C of L-shaped lever's short arm in system *Ovw* is marked as (v_c, w_c). Deduced from the relationship between the position of L-shaped lever and the deformation of plate spring, as shown in **Fig. 3**, it can be obtained that

$$v_c = \sqrt{l_2^2 - (h - \hat{x})^2} - \frac{l_1}{l_2}(h - \hat{x}) \tag{1}$$

$$w_c = \frac{l_1}{l_2}\sqrt{l_2^2 - (h - \hat{x})^2} - d \tag{2}$$

where $\hat{x} = x - z$ is the motion of isolation object relative to the base, $h = l_2\sqrt{1 - \left(\frac{d}{l_1}\right)^2}$ is the vertical distance between the long arm endpoints of L-shaped levers and the horizontal guiding shafts, in initial state.

As shown in **Fig. 3b**, when sliding on the surface of plate spring, the short arm end of L-shaped lever reaches arbitrary point between points O and C which is marked as $\mathrm{C}'(v,\ w)$, the arc length of the plate spring between the fixed endpoint O and point C' is marked as *s*. The bending angles of the plate spring relative to horizontal direction at points C' and C are denoted as β and β_c, respectively. The force acting on the point C of plate spring are F_c'. Correspondingly, the force acting on the short arm endpoint of L-shaped lever is F_c. Based on the Newton's third law of motion, regardless of the direction of the force, it can be derived that $F_c' = F_c$.

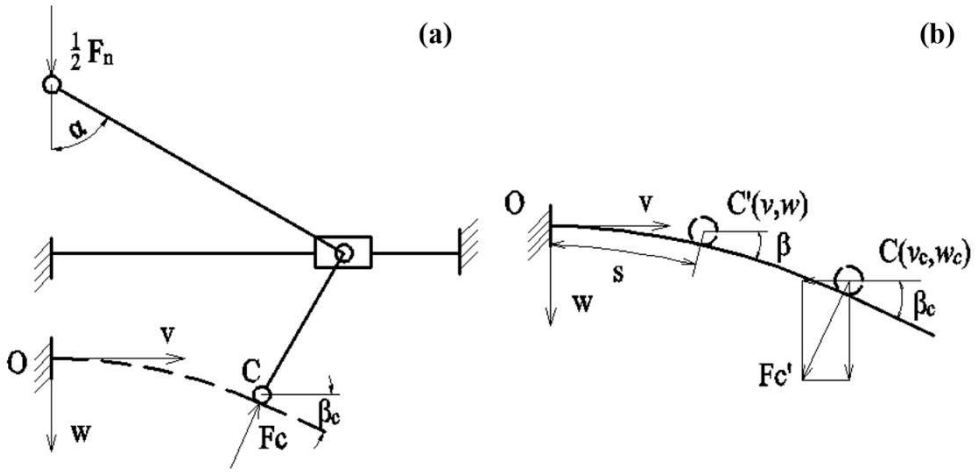


Fig. 3 Force and deformation diagrams of key parts: (a) L-shaped lever; (b) plate spring.

The plate spring, whose symmetrical center fixed on the base, can be approximated as two symmetrical arranged cantilever beams. The relationship between the bending moment and curvature for the plate spring at point C' can be expressed as [32-34],

$$\mathrm{EI}\frac{\mathrm{d}\beta}{\mathrm{d}s} = M \tag{3}$$

where E is the elastic modulus of plate spring, I is the moment of inertia of the plate spring cross section about the neutral axis, $\frac{\mathrm{d}\beta}{\mathrm{d}s}$ is the bending curvature of the plate spring at point C'. M is the bending moment acting on point C' of the plate spring, which can be expressed as below.

$$M = F_c'\cos\beta_c(v_c - v) + F_c'\sin\beta_c(w_c - w) \tag{4}$$

Both hand sides of Eq. (3) are differential with respect to *s*, getting that

$$\mathrm{EI}\frac{\mathrm{d}^2\beta}{\mathrm{d}s^2} = \frac{\mathrm{d}M}{\mathrm{d}s} \tag{5}$$

Substituting Eq. (4) into Eq. (5), derives that

$$\mathrm{EI}\frac{\mathrm{d}^2\beta}{\mathrm{d}s^2} + F_c'\cos\beta_c\cos\beta + F_c'\sin\beta_c\sin\beta = 0 \tag{6}$$

Considering the boundary conditions that $(\beta)_{s=L} = \beta_c$ and $\left(\frac{\mathrm{d}\beta}{\mathrm{d}s}\right)_{s=L} = 0$, the

differential arc length $\mathrm{d}s$ can be obtained by integrating the left-hand side of Eq. (6) with respect to s from *s* to *L* as

$$\mathrm{d}s = \sqrt{\frac{\mathrm{EI}}{2F_c'}}\frac{\mathrm{d}\beta}{\sqrt{\sin(\beta_c-\beta)}} \tag{7}$$

where *L* is the arc length of plate spring between points O and C.

Furthermore, projecting the arc length d*s* to the horizontal and vertical coordinates of the coordinate system *Ovw*, respectively, the differential length $\mathrm{d}v$ and $\mathrm{d}w$ can be obtained as expressed below.

$$\mathrm{d}v = \sqrt{\frac{\mathrm{EI}}{2F_c'}}\frac{\cos\beta\mathrm{d}\beta}{\sqrt{\sin(\beta_c-\beta)}} \tag{8}$$

$$\mathrm{d}w = \sqrt{\frac{\mathrm{EI}}{2F_c'}}\frac{\sin\beta\mathrm{d}\beta}{\sqrt{\sin(\beta_c-\beta)}} \tag{9}$$

Then, integrating Eqs. (8) and (9) with respect to β from 0 to β_c, respectively, the coordinates of point C (v_c, w_c) are obtained as shown in Eqs. (10) and (11).

$$\begin{aligned} v_c &= \sqrt{\frac{\mathrm{EI}}{2F_c'}}\left(2\cos\beta_c\sqrt{\sin\beta_c} + \sin\beta_c\int_0^{\beta_c}\sqrt{\sin\beta}\,\mathrm{d}\beta\right) \\ &\approx \sqrt{\frac{\mathrm{EI}}{2F_c'}}\left(2\cos\beta_c\sqrt{\sin\beta_c} + \frac{2}{3}\beta_c^{\frac{3}{2}}\sin\beta_c\right) \end{aligned} \tag{10}$$

$$\begin{aligned} w_c &= \sqrt{\frac{\mathrm{EI}}{2F_c'}}\left(2\sin\beta_c\sqrt{\sin\beta_c} - \cos\beta_c\int_0^{\beta_c}\sqrt{\sin\beta}\,\mathrm{d}\beta\right) \\ &\approx \sqrt{\frac{\mathrm{EI}}{2F_c'}}\left[2(\sin\beta_c)^{\frac{3}{2}} - \frac{2}{3}\beta_c^{\frac{3}{2}}\cos\beta_c\right] \end{aligned} \tag{11}$$

From Eqs. (10) and (11), it can be obtained that the bending angle β_c and the

force F_c are the functions of the coordinates of point C (v_c, w_c), which can be expressed as below.

$$\beta_c \approx -2\frac{v_c}{w_c} + \sqrt{4(\frac{v_c}{w_c})^2 + 6} \tag{12}$$

$$F_c = F_c{}' \approx \frac{2\mathrm{EI}\beta_c}{{v_c}^2} \tag{13}$$

Based on the principle of moment balance, the total moment acting on the elbow joint of each L-shaped lever can be obtained as

$$\frac{1}{2}F_n l_2 \sin\alpha + F_c \sin\beta_c l_1 \sin\alpha = F_c \cos\beta_c l_1 \cos\alpha \tag{14}$$

where F_n is the force acting on the NSE.

Combining Eqs. (1), (2), (12), (13) and (14), the restoring force of NSE, which is the function of relative displacement $\hat{x}$, can be written as

$$F_n = 4l_1 l_2 \frac{\mathrm{EI}\beta_c}{(l_2\sqrt{l_2^2-(h-\hat{x})^2}-l_1(h-\hat{x}))^2}(\cos\beta_c \frac{h-\hat{x}}{\sqrt{l_2^2-(h-\hat{x})^2}} - \sin\beta_c) \tag{15}$$

where

$$\beta_c = -2\frac{l_2\sqrt{l_2^2-(h-\hat{x})^2}-l_1(h-\hat{x})}{l_1\sqrt{l_2^2-(h-\hat{x})^2}-l_2 d} + \sqrt{4(\frac{l_2\sqrt{l_2^2-(h-\hat{x})^2}-l_1(h-\hat{x})}{l_1\sqrt{l_2^2-(h-\hat{x})^2}-l_2 d})^2 + 6} \tag{16}$$

Furthermore, according to the superposition principle of restoring forces of parallel connected springs, the restoring force F_q of the nonlinear isolator comprised of the NSE and linear springs can be obtained as below.

$$F_q = 4l_1 l_2 \frac{\mathrm{EI}\beta_c}{(l_2\sqrt{l_2^2-(h-\hat{x})^2}-l_1(h-\hat{x}))^2}(\cos\beta_c \frac{h-\hat{x}}{\sqrt{l_2^2-(h-\hat{x})^2}} - \sin\beta_c) + k\hat{x} \tag{17}$$

To facilitate calculation and analysis, we set new vertical displacement coordinate *u*, whose origin is on the plane formed by the centers of two horizontal guiding shafts,

as shown in **Fig. 2**. The relationship between u and x is $u=x-l_2\sqrt{1-\left(\frac{d}{l_1}\right)^2}$. And the displacement of supporting platform relative to the base in new coordinate system is expressed as $\hat{u}=\hat{x}-h=\hat{x}-l_2\sqrt{1-\left(\frac{d}{l_1}\right)^2}$. Define $k_{ref}=\frac{\mathrm{EI}}{l_1^3}$ as the equivalent stiffness of cantilever plate spring, which reflects the bearing capacity of the plate spring. And $F_{ref}=\frac{\mathrm{EI}}{l_1^2}$ is the force which is required to make the lateral deformation of the end of cantilever plate spring to be l_1.

Substituting $\hat{u}=\hat{x}-h$ into Eq. (15) and dividing both hand sides of Eq. (15) by F_{ref}, the non-dimensional force-displacement relationship of NSE can be obtained as,

$$\tilde{F}_n=\frac{-4}{\delta}\left(\sqrt{\delta^2-\tilde{u}^2}+\frac{1}{\delta}\tilde{u}\right)^{-2}\left(\cos\beta_c\frac{\tilde{u}}{\sqrt{\delta^2-\tilde{u}^2}}+\sin\beta_c\right)\beta_c \tag{18}$$

where $\beta_c=-2\frac{\delta\sqrt{\delta^2-\tilde{u}^2}+\tilde{u}}{\sqrt{\delta^2-\tilde{u}^2}-\delta\gamma}+\sqrt{4\left(\frac{\delta\sqrt{\delta^2-\tilde{u}^2}+\tilde{u}}{\sqrt{\delta^2-\tilde{u}^2}-\delta\gamma}\right)^2+6}$, $\tilde{F}_n=\frac{F_n}{F_{ref}}$ is the non-dimensional restoring force of NSE. $\tilde{u}=\frac{\hat{u}}{l_1}$ is the non-dimensional displacement of supporting platform relative to the base, $\delta=\frac{l_2}{l_1}$ is the length ratio of two arms of L-shaped lever, $\gamma=\frac{d}{l_1}$ is the non-dimensional distance between the fixed end of cantilever plate spring and the horizontal guiding shafts along vertical direction.

Similarly, the non-dimensional force-displacement relationship of the nonlinear isolator can be getting that

$$\tilde{F}_q=\frac{-4}{\delta}\left(\sqrt{\delta^2-\tilde{u}^2}+\frac{1}{\delta}\tilde{u}\right)^{-2}\beta_c\left(\cos\beta_c\frac{\tilde{u}}{\sqrt{\delta^2-\tilde{u}^2}}+\sin\beta_c\right)+\lambda\tilde{u}+\lambda\delta\sqrt{1-\gamma^2} \tag{19}$$

Where $\tilde{F}_q=\frac{F_q}{F_{ref}}$, $\lambda=\frac{k}{k_{ref}}$ is the equivalent stiffness ratio of vertical coil springs to plate spring.

Differentiating Eqs. (18) and (19) with respect to non-dimensional displacement $\tilde{u}$, the non-dimensional stiffness of the NSE and the nonlinear isolator can be

respectively derived as

$$\tilde{k}_n = \frac{8}{\delta}\left(\Delta + \frac{1}{\delta}\tilde{u}\right)^{-3}\left(-\frac{\tilde{u}}{\Delta} + \frac{1}{\delta}\right)\beta_c\left(\cos\beta_c\frac{\tilde{u}}{\Delta} + \sin\beta_c\right) - \frac{4}{\delta}\left(\Delta + \frac{1}{\delta}\tilde{u}\right)^{-2}\frac{\partial\beta_c}{\partial\tilde{u}}\left(\cos\beta_c\frac{\tilde{u}}{\Delta} + \sin\beta_c\right) + \frac{4}{\delta}\left(\Delta + \frac{1}{\delta}\tilde{u}\right)^{-2}\beta_c\left(\sin\beta_c\frac{\partial\beta_c}{\partial\tilde{u}}\frac{\tilde{u}}{\Delta} - \cos\beta_c\,\delta^2\Delta^{-3} - \cos\beta_c\frac{\partial\beta_c}{\partial\tilde{u}}\right) \tag{20}$$

$$\tilde{k}_q = \tilde{k}_n + \lambda \tag{21}$$

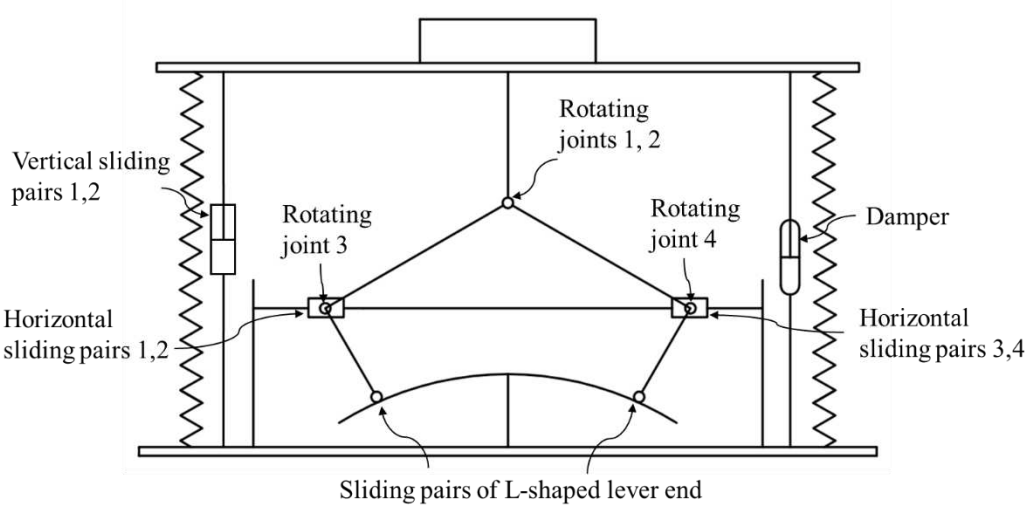
where

$$\Delta = \sqrt{\delta^2 - \tilde{u}^2} \tag{22}$$

$$\frac{\partial\beta_c}{\partial\tilde{u}} = \frac{2}{\Delta}\left(\frac{-\delta\tilde{u}+\Delta}{\Delta-\delta\gamma} + \frac{\delta\tilde{u}\Delta+\tilde{u}^2}{(\Delta-\delta\gamma)^2}\right)\left(\frac{2(\delta\Delta+\tilde{u})}{\sqrt{4(\delta\Delta+\tilde{u})^2+6(\Delta-\delta\gamma)^2}} - 1\right) \tag{23}$$

3.2 Nonlinear damping force model

The AQZS-VI comprised of several kinematic (sliding and rotating) pairs exhibits complex nonlinear damping property. Considering more generalized situation, the nonlinear damping force of the AQZS-VI produced by the Coulomb friction of kinematic pairs and by viscous friction of equivalent vertical damper are studied in the dynamic analysis of the vibration isolator. The equivalent vertical damper, sliding pairs and rotating joints of the AQZS-VI are depicted in Fig. 4. In the figure, it can be seen that the isolator consists of eight sliding and four rotating pairs. The twelve kinematic pairs respectively represent two vertical guiding rod-sleeve combinations, four horizontal guiding rod-sleeve combination, two sliding pairs between the bending plate spring and L-shaped levers, and four rotating joints. By means of the nonlinear geometric transformation, the Coulomb friction produced by each kinematic pair can be equivalent to the nonlinear vertical damping force.



284

285 **Fig. 4** The equivalent vertical damper, sliding pairs and rotating joints of the AQZS-VI.

286 The damping force of the equivalent vertical damper are defined as F_v which is
287 the linear function of relative vertical velocity $\frac{\mathrm{d}\tilde{u}}{\mathrm{d}t}$, written as

288 $$F_v = cl_1 \frac{\mathrm{d}\tilde{u}}{\mathrm{d}t} \tag{24}$$

289 where c is the viscous friction constant of equivalent vertical damper.

290 The vertical damping force F_{c1} caused by the friction of two vertical guiding
291 mechanisms can be expressed as

292 $$F_{c1} = 2\mu N_1 \mathrm{sgn}(\frac{\mathrm{d}\tilde{u}}{\mathrm{d}t}) = 2f_{c1}\mathrm{sgn}(\frac{\mathrm{d}\tilde{u}}{\mathrm{d}t}) \tag{25}$$

293 where μ is the friction resistance coefficient, N_1 the positive pressure between each
294 part of the vertical sliding pairs, f_{c1} the friction force in vertical direction. The value
295 of friction coefficient μ depends on the contact surface and material which can be
296 referred to handbook of engineering materials.

297 The equivalent vertical damping force F_{c2} induced by the friction of two
298 horizontal guiding mechanisms can be deduced [35] as

299 $$F_{c2} = 4\frac{\tilde{u}^2}{\delta^2-\tilde{u}^2}\mu N_2 \mathrm{sgn}(\frac{\mathrm{d}\tilde{u}}{\mathrm{d}t}) = 4\frac{\tilde{u}^2}{\delta^2-\tilde{u}^2} f_{c2}\mathrm{sgn}(\frac{\mathrm{d}\tilde{u}}{\mathrm{d}t}) \tag{26}$$

where N_2 is the positive pressure between contact surface of each horizontal guiding mechanism, f_{c2} the friction force in horizontal direction.

The equivalent vertical damping force F_{c3} caused by the friction of relative displacement between the short arm end of L-shaped lever and the bending plate spring can be obtained as

$$F_{c3} = 2\frac{1}{\delta}\left(\cos\beta_c - \sin\beta_c \frac{\tilde{u}}{\sqrt{\delta^2-\tilde{u}^2}}\right)\mu N_3 \mathrm{sgn}\left(\frac{\mathrm{d}\tilde{u}}{\mathrm{d}t}\right) = \frac{2}{\delta}\left(\cos\beta_c - \sin\beta_c \frac{\tilde{u}}{\sqrt{\delta^2-\tilde{u}^2}}\right) f_{c3}\mathrm{sgn}\left(\frac{\mathrm{d}\tilde{u}}{\mathrm{d}t}\right) \tag{27}$$

where N_3 is the positive pressure of contact surface between each short arm end of L-shaped lever and the bending plate spring, f_{c3} the friction force in the bending direction of plate spring.

The friction force of each rotating joint is

$$F_{c\varphi} = \mu N_4 \mathrm{sgn}[(\mathrm{d}\alpha/\mathrm{d}\hat{u})\cdot\dot{\hat{u}}] = f_{c4}\mathrm{sgn}(\dot{\hat{u}}) \tag{28}$$

where N_4 is the positive pressure (or tightening force) of joint, α the inclination angle of the long arm of the L-shaped lever relative to the vertical direction as shown in **Fig. 3,** f_{c4} the friction force in α direction.

The equivalent damping force acting on the vertical guiding mechanism caused by the friction of elbow joints of L-shaped levers (rotating joints 3 and 4, shown in Fig.4) is $F_{\varphi v} = 2F_{c\varphi}\sqrt{{l_2}^2 - \hat{u}^2}$. Meanwhile, the equivalent damping force acting on the horizontal guiding mechanism caused by the friction of long arm end joints of L-shaped levers (rotating joints 1 and 2, shown in Fig.4) is $F_{\varphi h} = -2\hat{u}F_{c\varphi}$. Therefore, the equivalent vertical damping force F_{c4} caused by the friction of four rotating joints is

$$F_{c4} = F_{\varphi v} + F_{\varphi h}\frac{-\hat{u}}{\sqrt{{l_2}^2-\hat{u}^2}} = 2\frac{\delta^2}{\delta^2-\tilde{u}^2}f_{c4}\mathrm{sgn}(\frac{\mathrm{d}\tilde{u}}{\mathrm{d}t}) \quad (29)$$

Finally, the total equivalent vertical damping force F_c produced by Coulomb friction of the sliding and rotating pairs can be sum up and written as

$$F_c = f_f\mathrm{sgn}(\frac{d\tilde{u}}{dt}) = (f_{f1}+f_{f2}+f_{f3}+f_{f4})\mathrm{sgn}(\frac{d\tilde{u}}{dt}) \quad (30)$$

where f_{f1}, f_{f2}, f_{f3} and f_{f4} respectively represent the equivalent vertical damping forces of two vertical guiding mechanisms, two horizontal guiding mechanisms, two contact surfaces between bending plate spring and two L-shaped levers, and four rotating joints, whose expressions are listed in (A.1-A.4) of **Appendix A**.

4. Nonlinear stiffness and damping properties

Based on the model established in Section 3, the nonlinear force-displacement and stiffness-displacement characteristics of the NSE and the nonlinear isolator are investigated in this section. And the equivalent Coulomb friction damping characteristics of the sliding and rotating pairs and their influence on the damping characteristics of the nonlinear isolator are also analyzed.

4.1 Nonlinear stiffness properties

4.1.1 Nonlinear stiffness of NSE

Based on the static model of the AQZS-VI established in Section 3.1, the nonlinear stiffness characteristics of NSE and their sensitivity to different parameters are analyzed in this section. The non-dimensional force–displacement characteristics of NSE for different length ratios (δ and γ) are calculated using Eq. (18) and plotted in **Fig. 5a** and **5c**. Similarly, the non-dimensional stiffness-displacement characteristics of NSE for different length ratios (δ and γ) are calculated using Eq. (20) and plotted in **Fig.**

5b and **5d**. As shown in **Fig. 2**, the relative displacement range of NSE we concerned is from the position $\hat{u} = -h$ (plate spring remains un-deformed) to the position $\hat{u} = h$ (plate spring returns to its un-deformed state). Correspondingly, the range of non-dimensional relative displacement $\tilde{u}$ is set from $-\frac{h}{l_1}$ to $\frac{h}{l_1}$ as plotted in **Fig. 5**.

From **Fig. 5a** and **5b**, it can be revealed that for a specific length ratio $\delta = 2$, the displacement range as well as the negative stiffness region increases with the decrease of γ. The smaller γ is, the stronger the nonlinear characteristic of the NSE is, and the lower negative stiffness can be obtained. Smaller γ is beneficial to get a relatively lower negative stiffness and larger negative stiffness region. In **Fig. 5a**, the restoring force of NSE increases rapidly at the beginning of the relative displacement stroke, then decreases slowly with the increase of the relative displacement, and finally increases at the end of the relative displacement stroke. In **Fig. 5c** and **5d**, the displacement range as well as the negative stiffness region increase with the increase of δ for a specific length ratio $\gamma = 0.75$. However, the smaller δ is, the stronger the nonlinear characteristic of the NSE is and the lower negative stiffness can be achieved. From **Fig. 5**, it can be concluded that the minimum negative stiffness (marked as $\tilde{k}_{n0}$) and its occurrence position (marked as $\tilde{u}_0$) are not fixed with the changing of γ and δ, while always appears between the upper limit point $\tilde{u}=-\frac{h}{l_1}$ and the center of two limit points $\tilde{u}=0$.

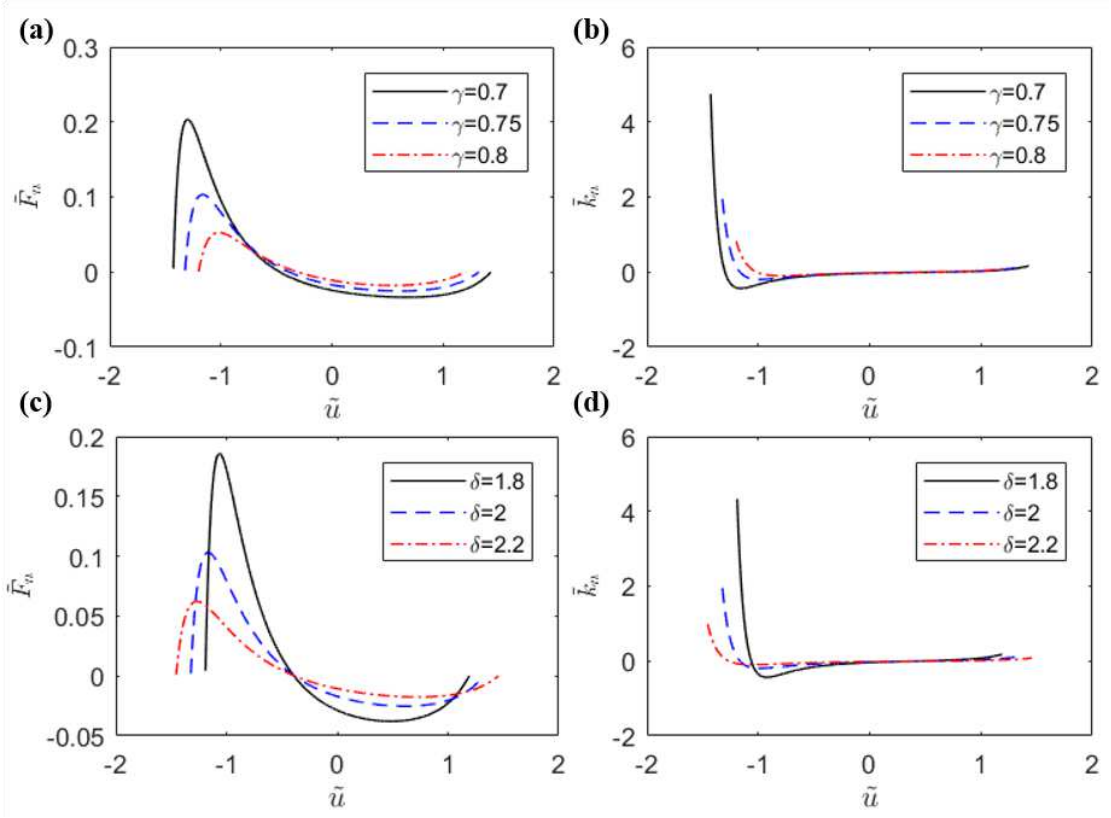


Fig. 5 The non-dimensional force-displacement (a) and stiffness-displacement (b) curves of the NSE for $\delta = 2$; The non-dimensional force-displacement (c) and stiffness-displacement (d) curves of the NSE for $\gamma = 0.75$.

4.1.2 Nonlinear stiffness of the proposed isolator

For $\delta = 2.2$ and $\gamma = 0.75$, the effects of different stiffness ratio λ on the static mechanical properties of the nonlinear isolator are plotted in **Fig. 6** based on Eqs. (19) and (21). The dynamic stiffness of the nonlinear isolator is largest at the initial position which corresponds to $\tilde{u} = -\frac{h}{l_1}$ and soon decrease rapidly with the increase of displacement. The minimum stiffness occurs at $\tilde{u}_0 = -1.0536$, which can be obtained by solving the equation $\frac{\partial \tilde{k}_n}{\partial \tilde{u}} = 0$ ($\frac{\partial \tilde{k}_n}{\partial \tilde{u}}$ can be obtained by differentiating Eq. (20) with respect to $\tilde{u}$). After the motion of the isolation platform reaches $\tilde{u}_0$, the stiffness increases slowly with the increase of the displacement. The increasing rate of the stiffness is much smaller than the initial decrease rate of stiffness, which exhibits

asymmetric property. The large stiffness and its decreasing rate during initial movement is beneficial for improving the bearing capacity with small displacement. While after the isolation platform reaches $\tilde{u}_0$, the small stiffness with slow increasing rate is helpful for achieving large displacement range under small stiffness value, which means that the isolator has a long working stroke.

The minimum stiffness can be changed from negative to positive with the increase of stiffness ratio λ as shown in **Fig. 6b**. If the stiffness ratio λ is chosen properly, the zero dynamic stiffness can be obtained at point $\tilde{u}_0$, of which $\tilde{u}_0$ is named as zero stiffness point (ZSP), and the nonlinear isolator becomes AQZS-VI. It's worth noting that the stiffness ratio λ can be increased by decreasing the flexural rigidity of the plate spring or increasing the stiffness of the vertical springs, and vice versa.

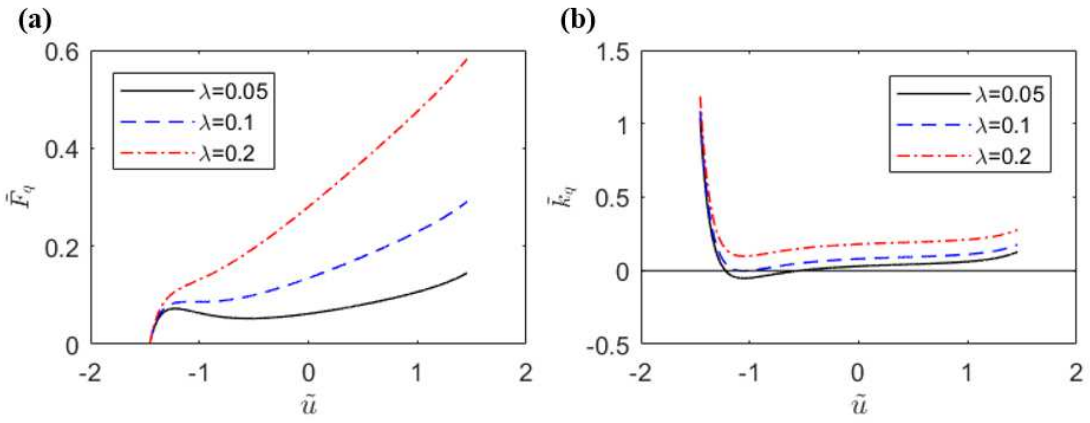


Fig. 6 Non-dimensional force-displacement (a) and stiffness-displacement (b) curves of the nonlinear isolator with different λ for $\delta = 2.2$ and $\gamma = 0.75$.

Different from symmetric QZS-VI whose NSE does not provide supporting force, the NSE of proposed AQZS-VI provides substantial supporting force at ZSP, which is beneficial for improving the bearing capacity of the nonlinear isolator. To reveal the contribution of the supporting force of the NSE to the bearing capacity of the vibration isolator, the non-dimensional restoring forces and stiffness of the AQZS-VI and its components: NSE and positive stiffness springs (PSSs) are plotted in same figure, as

shown in **Fig. 7**. From the figure, it can be seen that near ZSP, the non-dimensional restoring force of AQZS-VI is the sum of restoring forces of NSE and PSSs, of which the NSE provides larger restoring force than PSSs. The static supporting force of NSE is very beneficial for improving the bearing capacity of AQZS-VI.

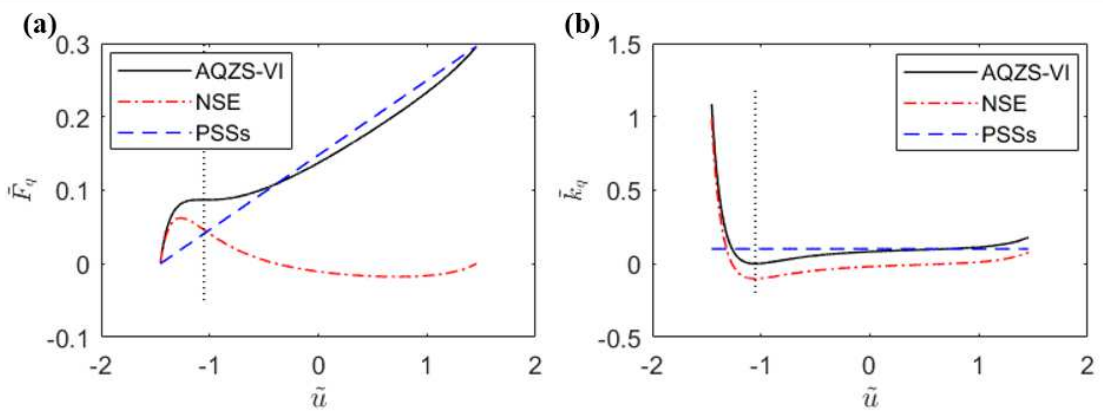


Fig. 7 Non-dimensional force-displacement (a) and stiffness-displacement (b) curves of the AQZS-VI, NSE and PSSs for $\delta = 2.2$, $\gamma = 0.75$ and $\lambda = 0.1$.

For different values of length ratios δ and γ, different stiffness ratio λ_0 are required to make the nonlinear isolator obtain zero dynamic stiffness ($\tilde{k}_q = 0$) at $\tilde{u}_0$. Specifically, the stiffness ratio λ_0 is a function of the length ratios δ and γ, whose relationship is plotted as shown in **Fig. 8a**. From **Fig. 8a**, it can be observed that the smaller the length ratios δ and/or γ, the larger the stiffness ratio λ_0 is needed to acquire zero dynamic stiffness for the nonlinear isolator. What's more, zero stiffness point $\tilde{u}_0$ is also related to the length ratios δ and γ, as shown in **Fig. 8b**, where $\tilde{u}_0$ increases with the decrease of δ and the increase of γ.

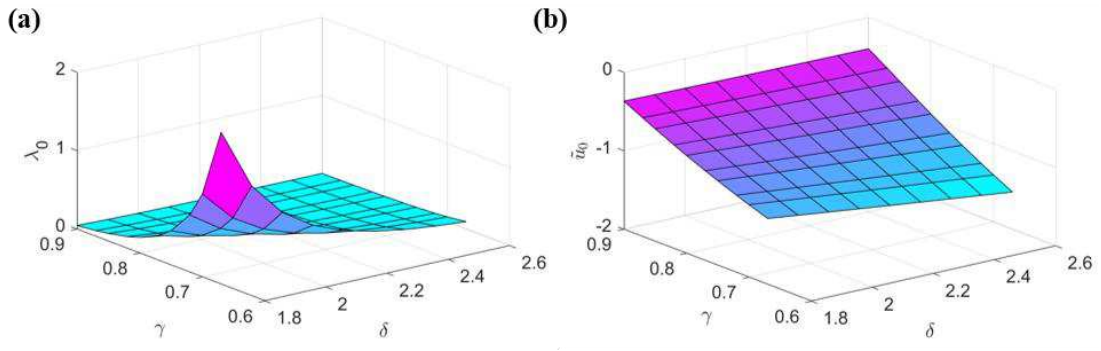


Fig. 8 The required stiffness ratio λ_0 (a) and zero stiffness point $\tilde{u}_0$ (b) with respect to different δ and γ for achieving zero dynamic stiffness at $\tilde{u}_0$.

4.2 Nonlinear damping properties

As shown in Fig.4, the isolator contains twelve kinematic pairs, of which the intrinsic nonlinearity of Coulomb friction combined with geometric nonlinearity constitutes complex nonlinear damping characteristics of the vibration isolator. As expressed in Section 3.2, Eq. (30) presents a nonlinear damping force which not only depends on the direction of motion but also on the structural parameters and relative displacement. This section focuses on the influence of different parameters on the nonlinear damping force of AQZS-VI. Considering general metal materials with smooth surface such as aluminum or steel, the friction forces set as for example $f_{c1} = 0.5$, $f_{c2} = 0.5$, $f_{c3} = 1$ and $f_{c4} = 1$. The values of equivalent vertical damping forces f_{f2}, f_{f3}, f_{f4} and f_f with respect to non-dimensional relative displacement under different length ratios δ and γ are shown in **Figs. 9** and **10**.

From **Fig. 9**, it can be seen that (1) for a specified value $\gamma = 0.75$, the damping forces f_{f2}, f_{f4} and f_f are decreasing functions of $\tilde{u}$ and they share very similar decreasing trend with the increase of relative displacement $\tilde{u}$, while $\tilde{u}$ has little effect on the damping force f_{f3}; (2) smaller δ leads to larger values of damping forces f_{f2}, f_{f3}, f_{f4} and f_f, and broaden the changing ranges of these damping forces along

the specified displacement range; (3) the total damping force f_f can be changed from a small value to a bigger one near ZSP $\tilde{u}_0$, which means AQZS-VI can dissipate more energy at the peak of resonant vibration.

Fig. 10 reveals the effect of length ratio γ on the damping forces f_{f2}, f_{f3}, f_{f4} and f_f. The nonlinear displacement-dependent properties of the damping forces are very clear. It is noticed that γ has no effect on f_{f2} and f_{f4}, while has little effect on f_{f3} and f_f. To obtain better nonlinear damping effect, it is necessary to further analyze the influence of structural parameters on linear and nonlinear damping properties.

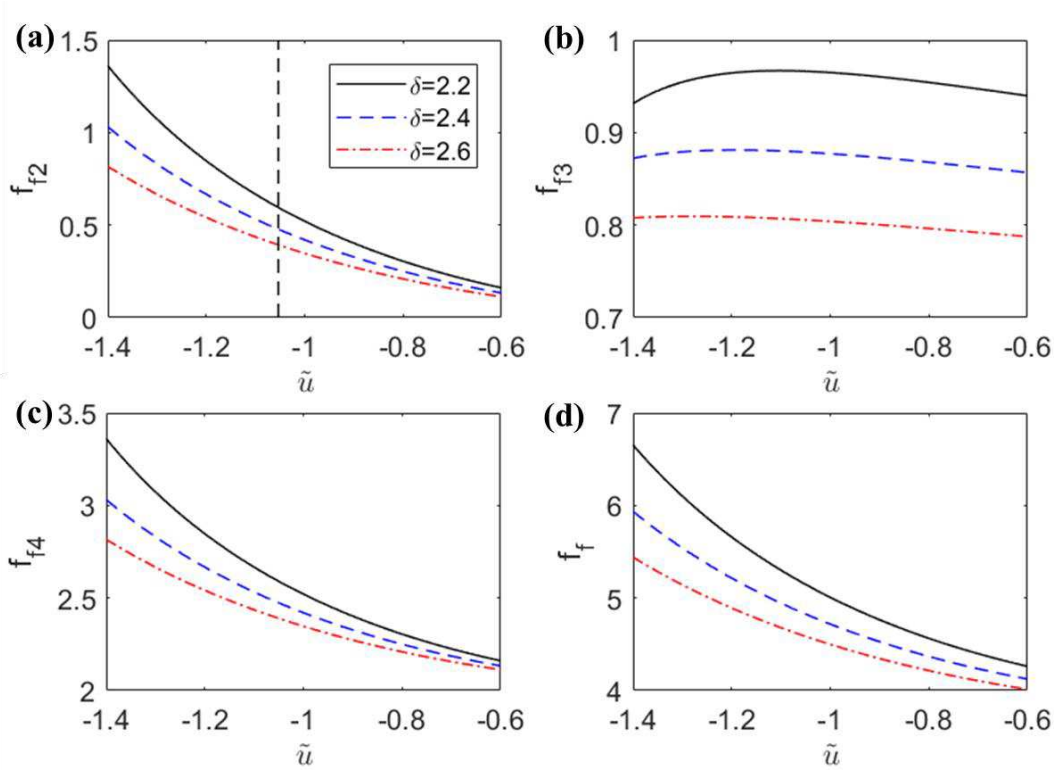


Fig. 9 The equivalent vertical damping forces f_{f2}, f_{f3}, f_{f4} and f_f for $\gamma = 0.75$ and different δ.

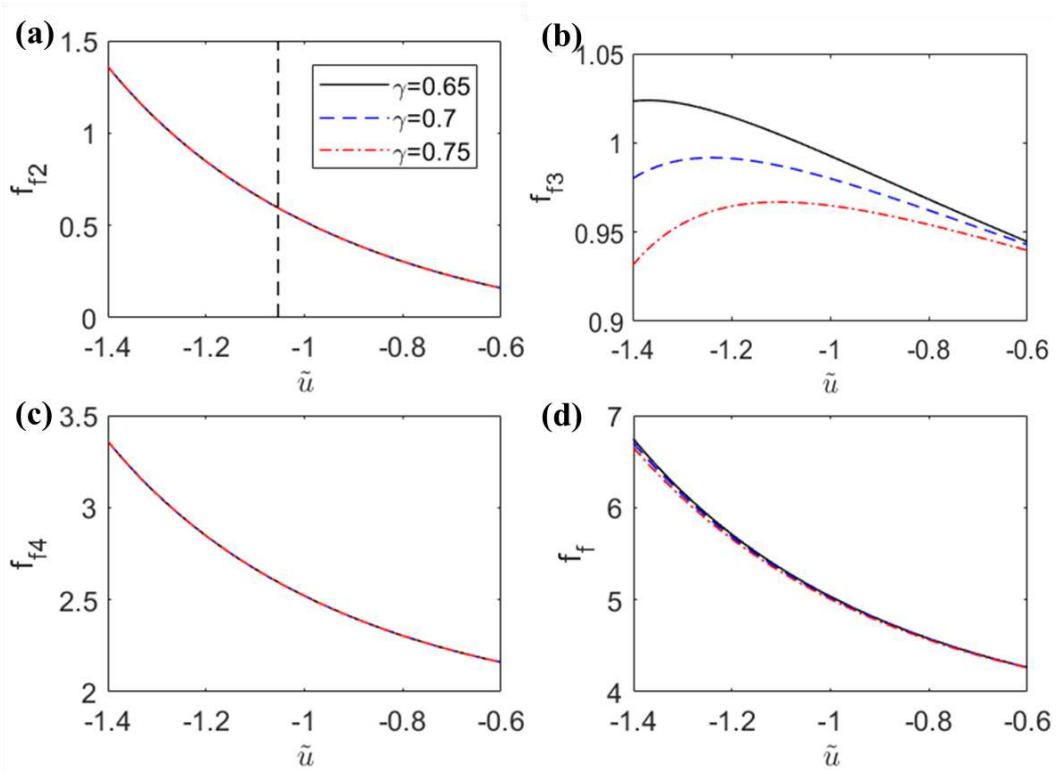


Fig. 10 The equivalent vertical damping forces f_{f2}, f_{f3}, f_{f4} and f_f for $\delta = 2.2$ and different γ.

From Eqs. (B.2-B.4), it can be seen obviously that f_{f2}, f_{f3} and f_{f4} are continuous at $\tilde{u} = \tilde{u}_0$, and they can be approximated by Taylor series expansion at ZSP as

$$f_{f2} = \varepsilon_0 + \varepsilon_1(\tilde{u} - \tilde{u}_0) + \varepsilon_2(\tilde{u} - \tilde{u}_0)^2 \tag{31}$$

$$f_{f3} = \varepsilon_3 + \varepsilon_4(\tilde{u} - \tilde{u}_0) + \varepsilon_5(\tilde{u} - \tilde{u}_0)^2 \tag{32}$$

$$f_{f4} = \varepsilon_6 + \varepsilon_7(\tilde{u} - \tilde{u}_0) + \varepsilon_8(\tilde{u} - \tilde{u}_0)^2 \tag{33}$$

where the expressions for $\varepsilon_0, \varepsilon_1, \varepsilon_2, \varepsilon_3, \varepsilon_4, \varepsilon_5, \varepsilon_6, \varepsilon_7$ and ε_8 are listed in A.5-A.13 of **Appendix A**. The total damping force f_f can be written as

$$f_f = \mu_0 + \mu_1(\tilde{u} - \tilde{u}_0) + \mu_2(\tilde{u} - \tilde{u}_0)^2 \tag{34}$$

where $\mu_0 = 2f_{c1} + \varepsilon_0 + \varepsilon_3 + \varepsilon_6$, $\mu_1 = \varepsilon_1 + \varepsilon_4 + \varepsilon_7$ and $\mu_2 = \varepsilon_2 + \varepsilon_5 + \varepsilon_8$.

It is obvious that μ_0, μ_1 and μ_2 are symbolically independent. The equivalent

total damping force expressed in Eq. (34) can be designed for proper nonlinear characteristic. This provides potentially effective way for nonlinear damping design with passive manner, which is attractive to engineering practice.

Setting the parameters of AQZS-VI as for example $\delta = 2.2$, $\gamma = 0.75$, $f_{c1} = 0.5$, $f_{c2} = 0.5$, $f_{c3} = 1$ and $f_{c4} = 1$, the comparison of Taylor series expansions and exact values of f_{f2}, f_{f3}, f_{f4} and f_f are shown in **Fig. 11**. From **Fig. 11**, it can be concluded that the Taylor expansion Eqs. (31-34) can basically represent the nonlinear damping forces near ZSP. **Fig. 11** also shows that the damping forces are asymmetric about $\tilde{u}_0$.

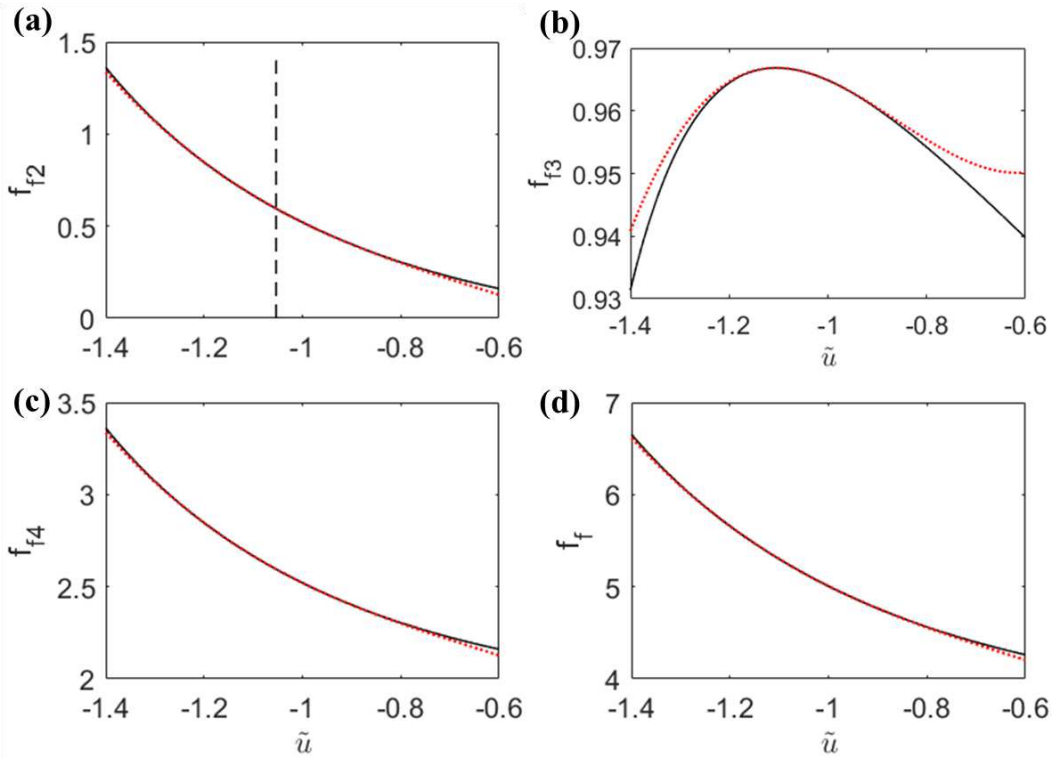
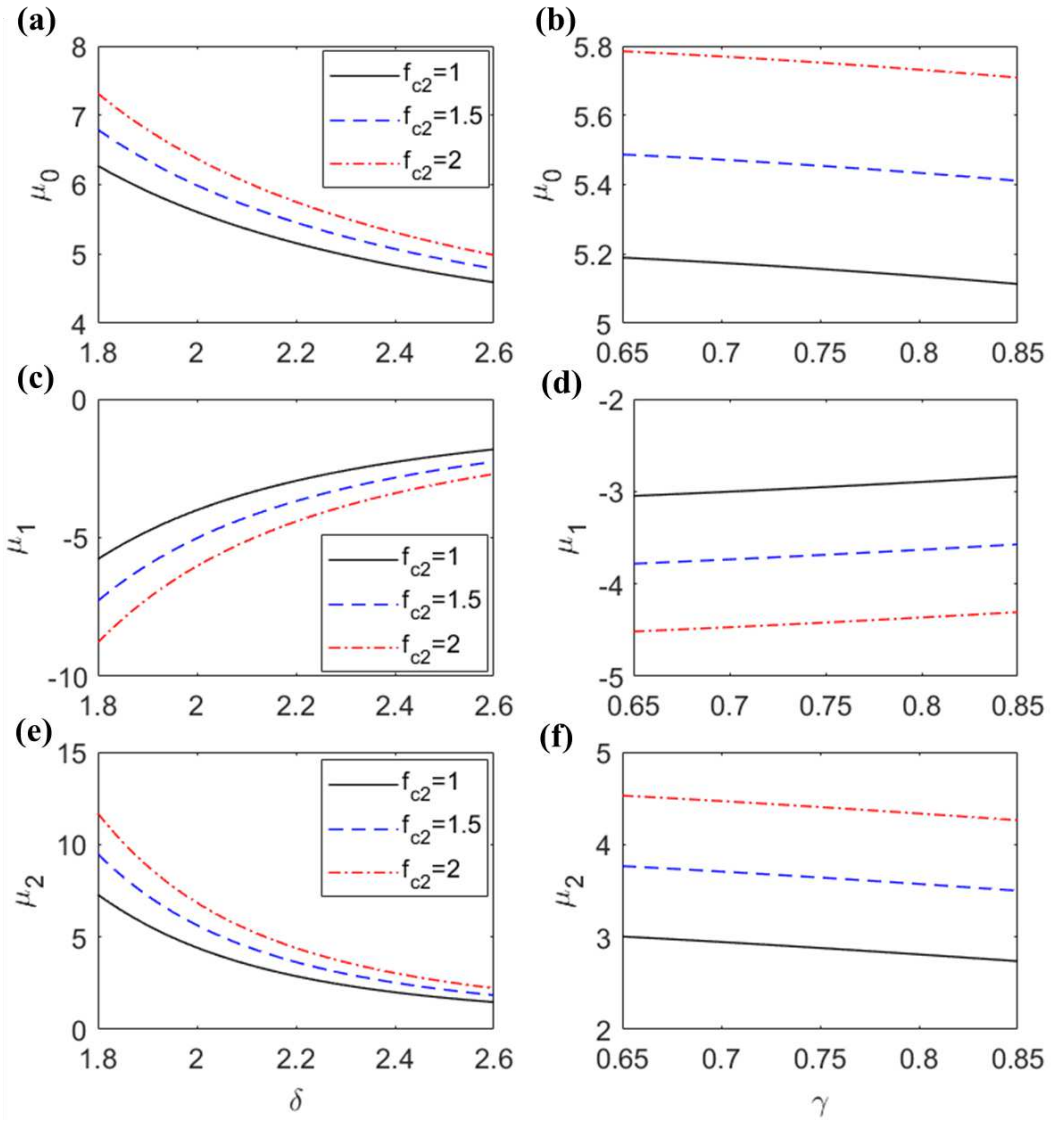


Fig. 11 Taylor expansion (dashed lines) compared with exact values (solid lines) of damping forces (a) f_{f2}, (b) f_{f3}, (c) f_{f4} and (d) f_f near ZSP $\tilde{u}_0$ (marked by vertical black dashed line).

The linear and nonlinear damping coefficients μ_0, μ_1 and μ_2 with different parameters δ, γ, f_{c2}, f_{c3} and f_{c4} are shown in **Figs. 12-14**. It can be seen from **Figs. 12** and **14** that the values of coefficients μ_0 and μ_2 are all positive, and decrease with

the increase of δ and γ and increase with the increase of f_{c2} and f_{c4}. The values of μ_0 and μ_2 are nearly linear decreasing functions of γ. The value of μ_1 is negative and increasing function of γ and δ, and decreasing function of f_{c2} and f_{c4}. From **Fig. 13**, μ_2 is the decreasing function of γ, whose decreasing rate increases with the increase of f_{c3}. While μ_2 is also the decreasing function of δ, which is seldom affected by f_{c3} under specified changing range of δ.

It is explicitly that the linear damping coefficient μ_0 is a linear increasing function of f_{c1} which can be altered independently. The increase of μ_0 is beneficial for vibration isolation near resonant frequency while deteriorate the isolation at higher frequencies. The nonlinear damping coefficients μ_1 and μ_2 are independent of f_{c1}. If linear damping is reduced for improving the high frequency isolation performance, nonlinear damping should be adjusted for enhancing the vibration isolation near resonant frequency [36]. It is practical to achieve such an advantageous damping property, although there exists coupling effect among nonlinear coefficients μ_1 and μ_2 when adjusting the same structural parameters. Proper optimization process could decouple the effect as the sensitivities of damping coefficients to different structural parameters are different.



487

488 **Fig. 12** The values of damping coefficient μ_0 under different f_{c2}, when (a) $\gamma = 0.75$ and (b)

489 $\delta = 2.2$; The values of μ_1 under different f_{c2}, when (c) $\gamma = 0.75$ and (d) $\delta = 2.2$; The values of μ_2

490 under different f_{c2}, when (e) $\gamma = 0.75$ and (f) $\delta = 2.2$.

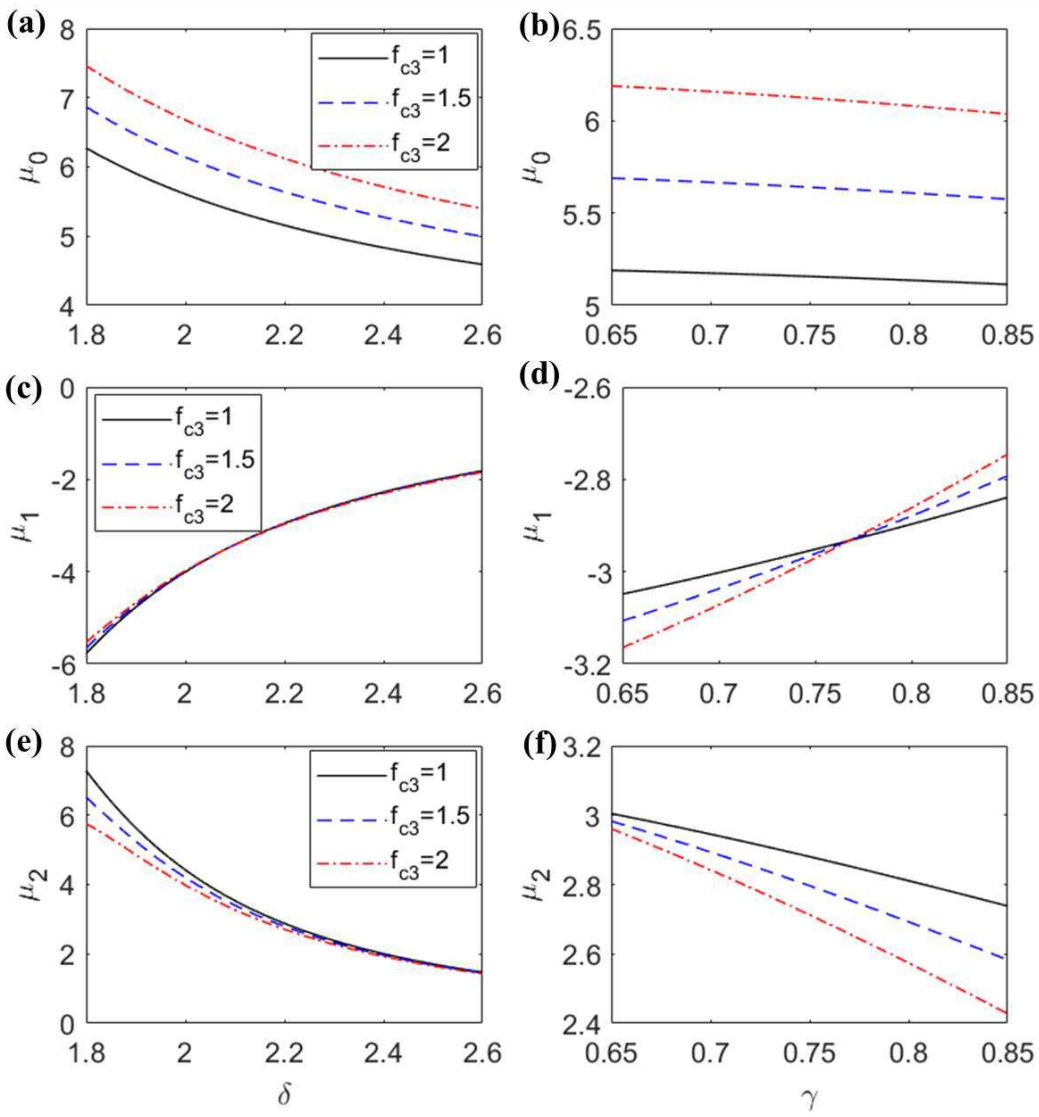


Fig. 13 The values of damping coefficient μ_0 under different f_{c3}, when (a) $\gamma = 0.75$ and (b) $\delta = 2.2$; The values of μ_1 under different f_{c3}, when (c) $\gamma = 0.75$ and (d) $\delta = 2.2$; The values of μ_2 under different f_{c3}, when (e) $\gamma = 0.75$ and (f) $\delta = 2.2$.

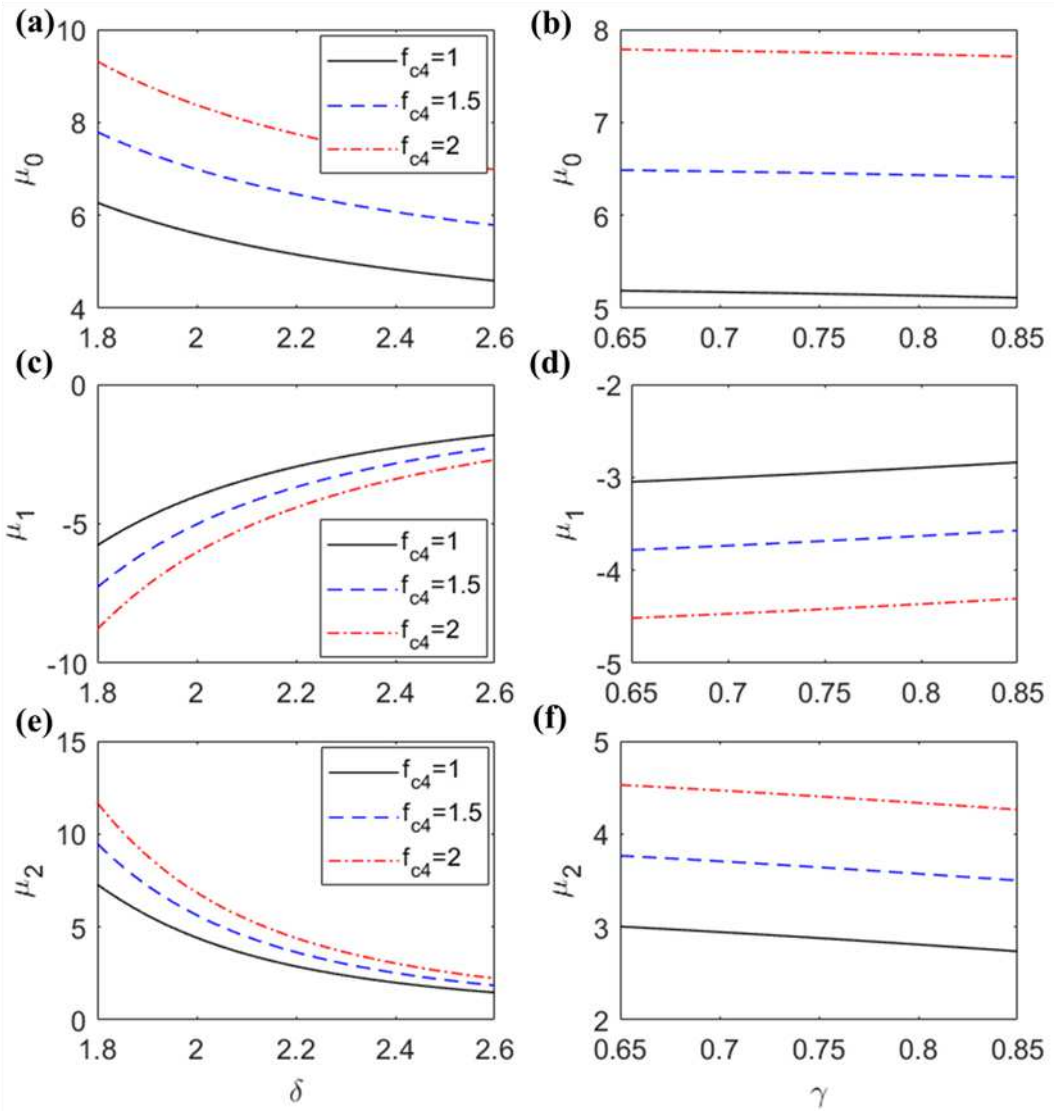
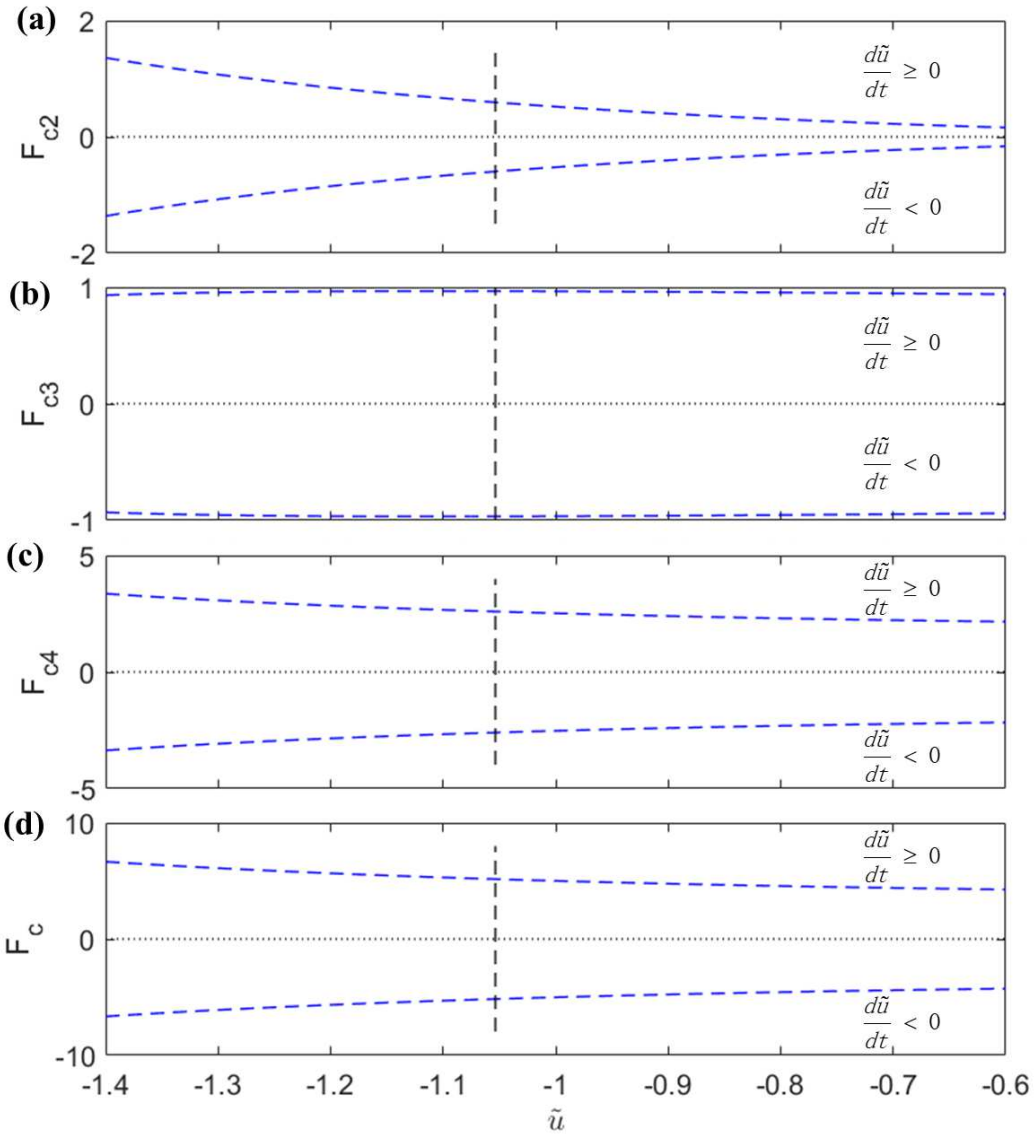


Fig. 14 The values of damping coefficient μ_0 under different f_{c4}, when (a) $\gamma = 0.75$ and (b) $\delta = 2.2$; The values of μ_1 under different f_{c4}, when (c) $\gamma = 0.75$ and (d) $\delta = 2.2$; The values of μ_2 under different f_{c4}, when (e) $\gamma = 0.75$ and (f) $\delta = 2.2$.

Considering the direction of friction force, the values of equivalent vertical damping forces F_{c2}, F_{c3} and F_{c4}, as well as the value of total equivalent vertical damping force F_c, near zero stiffness point $\tilde{u}_0$ are shown in Fig. 15. From the figure, it can be seen that the directions of the equivalent vertical damping forces are determined by the direction of the relative velocity $\frac{d\tilde{u}}{dt}$. The absolute values of F_{c2}, F_{c4} and F_c decrease with the increase of relative displacement $\tilde{u}$, while the F_{c3} is almost

unaffected by the relative displacement $\tilde{u}$. Although the friction of the isolator is energy dissipation caused by the relative motion of the contact surface, for large friction force, it is hard for the isolator to turn into the isolation state, which means that the isolation system is too rigid for excitation. Therefore, to reduce the values of equivalent vertical damping forces, one method is to smooth the surface of sliding and rotating pairs to reduce the values of f_{c1}, f_{c2}, f_{c3} and f_{c4}, and the other one is to increase the values of δ and γ. While the increasing of δ will decrease the zero stiffness point $\tilde{u}_0$, which is not conducive to the reduction of damping forces. The stiffness requirement of the isolator should be considered to determine the value of δ.



514

515 **Fig. 15** The equivalent vertical damping forces F_{c2}, F_{c3}, F_{c4} and F_c near ZSP $\tilde{u}_0$ (marked

516 by vertical black dashed line).

517 # 5. Displacement transmissibility

518 ## 5.1 Approximation of the restoring force

519 As discussed in Section 4.1, by choosing proper structural parameters, the

520 minimum dynamic stiffness of the nonlinear isolator can be designed to be zero at ZSP

521 $\tilde{u}_0$, which makes the nonlinear isolator to be AQZS-VI. The non-dimensional restoring

force of the AQZS-VI expressed by Eq. (19) are continuous near $\tilde{u}_0$ which can be expanded by Taylor series at $\tilde{u}_0$. The fifth order Taylor series expansion of Eq. (19) are shown as

$$\tilde{F}_q = \varphi_0 + \varphi_1(\tilde{u} - \tilde{u}_0) + \varphi_2(\tilde{u} - \tilde{u}_0)^2 + \varphi_3(\tilde{u} - \tilde{u}_0)^3 + \varphi_4(\tilde{u} - \tilde{u}_0)^4 + \varphi_5(\tilde{u} - \tilde{u}_0)^5 + o(\tilde{u}) \tag{35}$$

where $\varphi_0 = \tilde{F}_q(\tilde{u}_0)$, $\varphi_1 = \tilde{k}_q(\tilde{u}_0)$, $\varphi_2 = \frac{1}{2}\frac{\partial \tilde{k}_q}{\partial \tilde{u}}(\tilde{u}_0)$, $\varphi_3 = \frac{1}{6}\frac{\partial^2 \tilde{k}_q}{\partial \tilde{u}^2}(\tilde{u}_0)$, $\varphi_4 = \frac{1}{24}\frac{\partial^3 \tilde{k}_q}{\partial \tilde{u}^3}(\tilde{u}_0)$, $\varphi_5 = \frac{1}{120}\frac{\partial^4 \tilde{k}_q}{\partial \tilde{u}^4}(\tilde{u}_0)$, o is the higher order terms of $\tilde{u}$.

For the parameters setting as $\delta = 2.2$, $\gamma = 0.75$, it can be obtained that $\lambda_0 = 0.1$, $\tilde{u}_0 = -1.0536$. The relationship between the non-dimensional restoring forces and displacement, expressed by Eqs. (29) and (35), are plotted in same figure for comparison as shown in **Fig. 16**. It can be seen that the values of non-dimensional force are asymmetric about $\tilde{u}_0$ and the approximation curve can fit the exact curve well near $\tilde{u}_0$. While with the relative displacement goes far away from $\tilde{u}_0$, the fitting accuracy becomes worse. Higher order expansion can improve the fitting accuracy, and fifth order expansion can better fit the exact curve and reflect the asymmetric properties of restoring force than third order expansion.

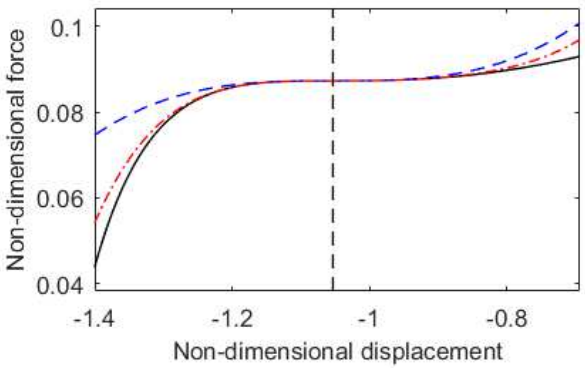


Fig. 16 Non-dimensional restoring force-displacement curves of the AQZS near ZSP $\tilde{u}_0$ for $\gamma =$

0.75 and $\delta = 2.2$: '-'exact solution; '--' third order expansion; '-·-' fifth order expansion. $\tilde{u}_0$ is marked by vertical black dashed line.

5.2 Dynamic model

It is instructive to note that the moving components of the CPS-LSL, including two L-shaped levers and two horizontal guide sleeves, can be constructed by high strength and low-density materials (carbon fiber or aluminum alloy, etc.). Two arms of each L-shaped lever can be designed to be hollow rods to minimize the flexibility and inertia influence on dynamic properties of the nonlinear isolator. The payload mass of the AQZS is assumed to be *m* which can make the isolator keep balance at ZSP $\tilde{u}_0$. The mass of two horizontal guide sleeves and the moment of inertia of two L-shaped levers are much smaller than the mass of isolation object, which can be neglected during the dynamic modeling of the AQZS-VI. To simplify modeling, the inertia effect of the internal moving parts of the vibration isolator on its own dynamic characteristics is ignored. As discussed in Section 3, the nonlinear isolator can be regarded as a single degree of freedom (SDOF) system, whose static mechanical equation is

$$F_{ref}\tilde{F}_q(\tilde{u}_0) - mg = 0 \tag{36}$$

Consider that the displacement excitation $z = Z_0\cos\omega t$ is exerted on the base of the AQZS-VI. Using Newton's second law of motion, the dynamic equations of the AQZS-VI is given as

$$ml_1\frac{\mathrm{d}^2\tilde{u}}{\mathrm{d}t^2} + F_c + F_v + F_{ref}\tilde{F}_q - mg = mZ_0\omega^2\cos\omega t \tag{37}$$

Substituting Eqs. (30), (35) and (36) into Eq. (37) and conducting a series of transformation, the non-dimensional dynamic equation is derived as

$$\frac{\mathrm{d}^2\tilde{u}}{\mathrm{d}\tau^2} + 2\xi_c f_d\,\mathrm{sgn}\left(\frac{\mathrm{d}\tilde{u}}{\mathrm{d}\tau}\right) + 2\xi_v\frac{\mathrm{d}\tilde{u}}{\mathrm{d}\tau} + f_q = \Omega^2 z_0\cos\Omega\tau \tag{38}$$

where $\omega_n = \sqrt{\frac{k_{ref}}{m}}$, $\tau = \omega_n t$, $\Omega = \frac{\omega}{\omega_n}$ is the frequency ratio, $\xi_c = \frac{f_{c1}}{2m\omega_n}$ is the damping factor of Coulomb friction, $\xi_v = \frac{c}{2m\omega_n}$ is the damping factor of equivalent viscous friction, $z_0 = \frac{Z_0}{l_1}$ is the non-dimensional amplitude of displacement excitation, $f_d = \frac{1}{f_{c1}} f_f$ is the non-dimensional damping coefficient expressed as

$$f_d = 2 + \frac{4f_{c2}}{f_{c1}}\frac{\tilde{u}^2}{\Delta^2} + \frac{2f_{c3}}{f_{c1}}\frac{1}{\delta}\left(\cos\beta_c - \sin\beta_c \frac{\tilde{u}}{\Delta}\right) + \frac{2f_{c4}}{f_{c1}}\frac{\delta^2}{\Delta^2} \tag{39}$$

And f_q is the non-dimensional restoring force of AQZS-VI, whose expression is

$$f_q = \varphi_1(\tilde{u} - \tilde{u}_0) + \varphi_2(\tilde{u} - \tilde{u}_0)^2 + \varphi_3(\tilde{u} - \tilde{u}_0)^3 + \varphi_4(\tilde{u} - \tilde{u}_0)^4 + \varphi_5(\tilde{u} - \tilde{u}_0)^5 \tag{40}$$

The non-dimensional damping coefficient f_d is a nonlinear function of $\tilde{u}$, which can be expanded by Taylor series. Compared with Eq. (34), the Taylor expansion of f_d at $\tilde{u}_0$ is

$$f_d = \mu_{10} + \mu_{11}(\tilde{u} - \tilde{u}_0) + \mu_{12}(\tilde{u} - \tilde{u}_0)^2 \tag{41}$$

where $\mu_{10} = \frac{1}{f_{c1}}\mu_0$, $\mu_{11} = \frac{1}{f_{c1}}\mu_1$, $\mu_{12} = \frac{1}{f_{c1}}\mu_2$.

The supporting platform vibrates up and down near the equilibrium point $\tilde{u}_0$. For the facility of dynamic analysis, we define a new non-dimensional displacement coordinate $\tilde{y}$, where $\tilde{u}_0$ is the origin of the coordinate system. Then the relationship between $\tilde{y}$ and $\tilde{u}$ is $\tilde{y} = \tilde{u} - \tilde{u}_0$. Substituting the Taylor series expansion Eqs. (40) and (41) into Eq. (38), the dynamic equation of the AQZS-VI can be given as

$$\tilde{y}'' + 2\xi_c(\mu_{10} + \mu_{11}\tilde{y} + \mu_{12}\tilde{y}^2)\mathrm{sgn}(\tilde{y}') + 2\xi_v\tilde{y}' + \varphi_1\tilde{y} + \varphi_2\tilde{y}^2 + \varphi_3\tilde{y}^3 + \varphi_4\tilde{y}^4 + \varphi_5\tilde{y}^5 = \eta e_0 \cos\Omega\tau \tag{42}$$

where $(\cdot)' = \mathrm{d}(\cdot)/\mathrm{d}\tau$.

The Harmonic Balance Method (HBM) [37] is used to solve the Eq. (42). As the equivalent stiffness and damping of AQZS-VI are asymmetric about zero stiffness point, the zero shift of vibration is considered and the solution of Eq. (42) can be set as

$$\tilde{y} = a_0 + a\ \cos(\Omega\tau + \varphi) \tag{43}$$

where a is the amplitude of harmonic term and a_0 is the zero shift known as bias term. The equations for a, a_0 and φ obtained by applying HBM are listed by (B. 1-B. 3) in **Appendix B**. From Eqs. (B. 1-B. 3) and the trigonometric identity: $\sin^2\varphi + \cos^2\varphi = 1$, the absolute displacement transmissibility T_d for displacement excitation can be derived as

$$T_d = \left|\frac{\sqrt{a^2 + {z_0}^2 + 2az_0\cos\varphi}}{z_0}\right| \tag{44}$$

5.3 Effects of excitation amplitude and damping on the transmissibility

For a nonlinear vibration isolation system, the excitation amplitude and damping have great influence on its response [37]. In this section, the vibration transmissibility of the proposed AQZS-VI under displacement excitation is analyzed. During investigation the structural parameters which determine the property of the isolator are chosen for example as $\delta = 2.2,\ \gamma = 0.75,\ \lambda_0 = 0.1,\ \tilde{u}_0 = -1.0536,\ \frac{f_{c2}}{f_{c1}} = 1,\ \frac{f_{c3}}{f_{c1}} = 2$ and $\frac{f_{c4}}{f_{c1}} = 2$. Different excitation amplitudes and damping factors are imposed to study the vibration isolation performance of the AQZS-VI.

5.3.1 Effects of excitation amplitudes

In this section, the damping factors are fixed as $\xi_v = 0.025$ and $\xi_c = 0$. The absolute displacement transmissibility of the AQZS-VI under different amplitudes of displacement excitation are illustrated in **Fig. 17**. The figure depicts that the AQZS-VI

is a harden spring system for which the transmissibility-frequency curves near resonant frequency bend to the right-hand sides with the increase of displacement excitation amplitude. The displacement transmissibility is highly sensitive to the amplitude of displacement excitation near resonant frequency and the unbounded response occurs as the displacement excitation amplitude increases slightly. It is clear that the resonant frequency of AQZS-VI is lower than 0.1 times of ω_n, which is expected to achieve ultra-low frequency vibration isolation for the isolator.

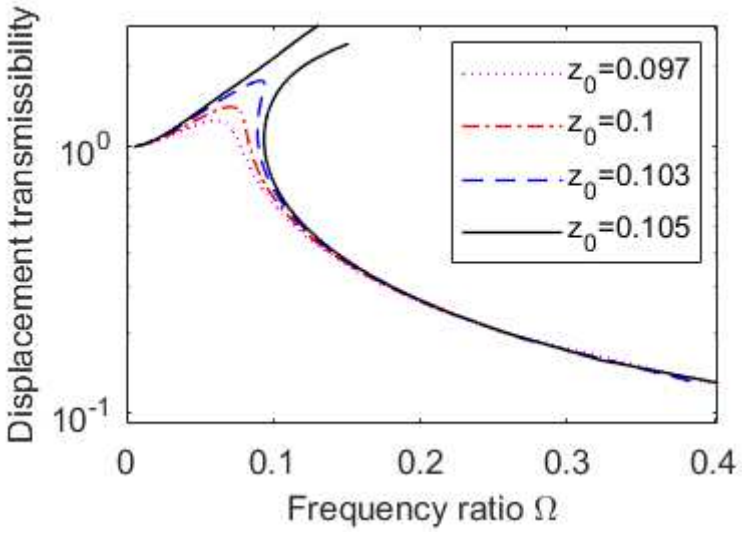


Fig. 17 Displacement transmissibility of the AQZS-VI under different amplitudes of excitation z_0 with $\xi_v = 0.025$, $\xi_c = 0$.

5.3.2 Effects of damping factors

The non-dimensional amplitude of displacement excitation is set as $z_0 = 0.1$ and the damping factor of Coulomb friction is fixed as $\xi_c = 0$. The absolute displacement transmissibility of AQZS-VI under different damping factors of viscous friction ξ_v are shown in **Fig. 18**. From **Fig. 18**, it can be obtained that the displacement transmissibility is highly sensitive to the value of damping factor ξ_v. The unbounded displacement transmissibility occurs with the decrease of damping factor ξ_v. Increasing the damping

factor ξ_v can prominently decreases the displacement transmissibility near resonant frequency, while increases the transmissibility at higher frequencies, which is similar to the performance of linear vibration isolator.

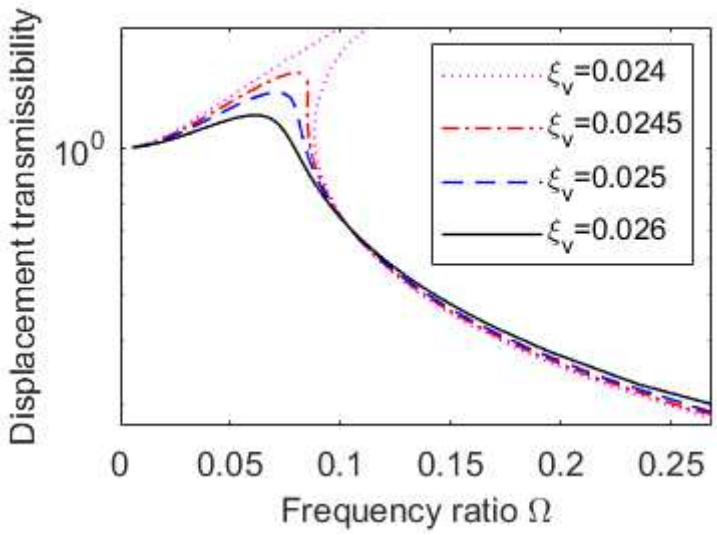


Fig. 18 Displacement transmissibility of the AQZS-VI under different damping factors of viscous friction ξ_v with $z_0 = 0.1$, $\xi_c = 0$.

Coulomb friction is the main source of damping force in the vibration isolator. It is of great significance to study the influence of Coulomb friction on the vibration isolation performance of the isolator. The absolute displacement transmissibility of AQZS-VI under different damping factors of Coulomb friction ξ_c are studied and the results are shown in **Fig. 19**. In the figure, the non-dimensional amplitude of displacement excitation is set as $z_0 = 0.1$ and the damping factor of viscous friction as $\xi_v = 0.025$. It can be seen that when the Coulomb friction force exists, i.e., $\xi_c > 0$, the rigid motion occurs in the low-frequency band of which the displacement transmissibility equals to 1. With the increase of ξ_c, the frequency band of rigid motion broaden and the resonance peak decreases until it disappears. The large Coulomb friction force (e.g., $\xi_c = 4 \times 10^{-5}$) makes the vibration isolator moves rigidly in the frequency region where the resonance may occur, increases the starting frequency of

vibration isolation and deteriorates the displacement transmissibility of the vibration isolator in higher frequencies.

As the Coulomb frictions exist in the kinematic pairs of the isolator, the supporting platform don't move relative to the base of the vibration isolator when the excitation force is less than the friction force of AQZS-VI, in other words, the self-locking occurs. Although the frictions of the kinematic pairs in the isolator have damping effect, it is very dangerous for a vibration isolator with rigid motion, especially for high-frequency excitation. Therefore, to avoid the rigid movement of the AQZS-VI and reduce the starting frequency of vibration isolation, it is beneficial to reduce the value of Coulomb friction in the kinematic pairs of the system.

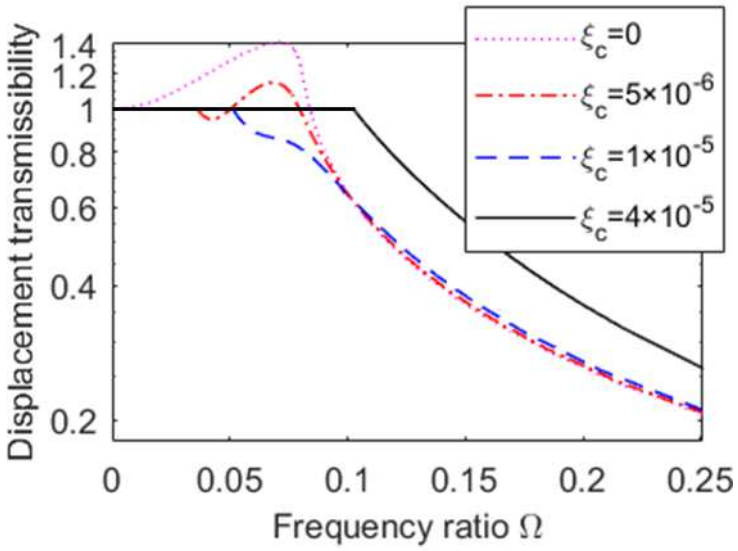


Fig. 19 Displacement transmissibility of the AQZS-VI under different damping factors of Coulomb friction ξ_c with $z_0 = 0.1$, $\xi_v = 0.025$.

6. Comparisons with existing vibration isolators

To objectively evaluate the static mechanical property and vibration isolation performance of the proposed AQZS-VI, the comparisons of static and dynamic properties between the proposed AQZS-VI, linear mass-spring-damping vibration

isolator (Linear VI) and symmetric QZS-VI (SQZS-VI) are conducted in this section.

6.1 Static mechanical properties comparison

A typical vibration isolator comprising two oblique springs acting in parallel with one vertical spring studied in the literatures [12] and [13] is chosen as the SQZS-VI for comparison. The non-dimensional restoring force $\hat{f}$ and stiffness $\hat{\mathrm{k}}$ of the SQZS-VI are expressed as

$$\hat{f} = \hat{x} + 2\alpha\left(\sqrt{1-\gamma^2} - \hat{x}\right)\left\{\left[\hat{x}^2 - 2\sqrt{1-\gamma^2}\hat{x} + 1\right]^{-\frac{1}{2}} - 1\right\} \quad (45)$$

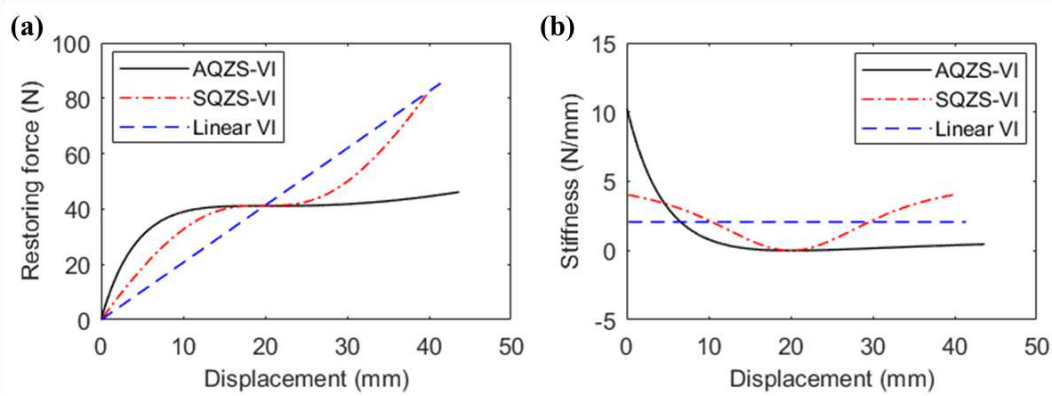
$$\hat{\mathrm{k}} = 1 + 2\alpha\left[1 - \frac{\gamma^2}{(\hat{x}^2 - 2\sqrt{1-\gamma^2}\hat{x}+1)^{3/2}}\right] \quad (46)$$

where $\hat{x} = \frac{x}{L_0}$ is the non-dimensional displacement, $\gamma = \frac{a}{L_o} = \cos\theta_0$ is the cosine of the initial inclination angle of two oblique springs, k_o is the stiffness of oblique spring, L_o is the initial length of oblique spring, $\alpha = \frac{k_o}{k_v}$ is stiffness ratio of oblique spring to vertical spring. It is worth noting that the value of α that ensures quasi-zero stiffness behavior for a given γ is

$$\alpha_{QZS} = \frac{\gamma}{2(1-\gamma)} \quad (47)$$

To facilitate comparison, the three isolators are set to have the same bearing capacity (m=4.21 kg) under same deformation (x = 20 mm). Specifically, set the parameters of SQZS-VI as $\gamma = 0.6$, $L_o = \frac{x}{\sqrt{1-\gamma^2}} = \frac{20}{\sqrt{1-0.6^2}} = 25$ mm and $k_o = \frac{mg}{\sqrt{1-\gamma^2}L_o} = 2.0625$ N mm^{-1} which are the optimized parameters. The parameters of AQZS-VI are $\delta = 2.2$, $\gamma = 0.75$, $\lambda_0 = 0.1016$, $\tilde{u}_0 = -1.0536$, l_1 =50 mm, l_2=110 mm, $k_{ref} = \frac{EI}{l_1^3} = 9.45$ N mm^{-1}, $F_{ref} = \frac{EI}{l_1^2} = 472.5$ N. The spring stiffness of Linear VI is $k_l = 2.0625$ N mm^{-1}. The restoring forces of three vibration isolators with respect to the displacement are plotted in same figure as shown in **Fig.**

683 **20a**. Correspondingly, the stiffness of three vibration isolators with respect to the
684 displacement are plotted in **Fig. 20b**.



685

686 **Fig. 20** The restoring force-displacement (a) and stiffness-displacement (b) curves of three isolators.

687 From **Fig. 20**, it can be concluded that the restoring forces and stiffness of SQZS-
688 VI and Linear VI are symmetric about the zero stiffness point (ZSP) of SQZS-VI (x=20
689 mm), while the restoring force and stiffness of AQZS-VI are asymmetric. The proposed
690 AQZS-VI has larger initial dynamic stiffness than SQZS-VI and the dynamic stiffness
691 decreases more rapidly than that of SQZS-VI during initial deformation. With the
692 displacement increased, the dynamic stiffness of AQZS-VI changes slower and
693 maintains smaller value than that of SQZS-VI in the neighborhood of ZSP. And after
694 the isolation platform reaches ZSP, the stiffness of AQZS-VI maintains low value and
695 increases much slower than that of SQZS-VI. The displacement range of AQZS-VI with
696 low dynamic stiffness is much larger than that of SQZS-VI. In a word, with the same
697 bearing capacity, the AQZS-VI has much longer working stroke than the SQZS-VI for
698 low frequency vibration isolation.

699 6.2 Dynamic mechanical properties comparison

700 The comparison of absolute displacement transmissibility between the AQZS-VI,
701 the SQZS-VI and the Linear VI under harmonic displacement excitations ($z_0 = 0.1$)
702 are conducted in this section. For a traditional linear vibration isolator with payload

mass m, linear spring stiffness k_l and damping constant c_l, its dynamic equations under harmonic displacement excitation (z=$Z_0\cos\omega t$) can be written as

$$\frac{\mathrm{d}^2\tilde{y}}{\mathrm{d}\tau^2}+2\xi_l\frac{\mathrm{d}\tilde{y}}{\mathrm{d}\tau}+\tilde{y}=\Omega^2 z_0\cos\Omega\tau \quad (48)$$

Where $\omega_{nl}=\sqrt{\frac{k_l}{m}}$, $\tau=\omega_{nl}t$, $\Omega=\frac{\omega}{\omega_{nl}}$, $\xi_l=\frac{c_l}{2m\omega_{nl}}$, $\tilde{y}=\frac{y}{l_0}$, $z_0=\frac{Z_0}{l_0}$, l_0 is the reference length of linear spring, y is the displacement of payload relative to the base of Linear VI.

The dynamic equations of the SQZS-VI under displacement excitation (z=$Z_0\cos\omega t$) are given by

$$\frac{\mathrm{d}^2\hat{x}}{\mathrm{d}\tau^2}+2\xi_s\frac{\mathrm{d}\hat{x}}{\mathrm{d}\tau}+\hat{f}-\frac{mg}{k_o L_o}=z_0\Omega^2\cos\Omega\tau \quad (49)$$

where $\omega_{ns}=\sqrt{\frac{k_o}{m}}$, $\tau=\omega_{ns}t$, $\Omega=\frac{\omega}{\omega_{ns}}$, $\xi_s=\frac{c_s}{2m\omega_{ns}}$, $z_0=\frac{Z_0}{L_o}$, $\hat{x}=\frac{x}{L_0}$ is the non-dimensional relative displacement of payload respect to the base of SQZS-VI. m, c_s, k_o are respectively represent the payload mass, damping constant of viscous damper and stiffness of oblique spring. $\hat{f}$ is the non-dimensional restoring force of the SQZS-VI, whose expression is shown in Eq. (45).

The parameters of the three isolators are set to be equal to that specified in Section 6.1. In addition, the three isolators are specified to have same damping properties. Specifically, for AQZS-VI, the Coulomb friction is ignored and only consider viscous friction, i.e., $\xi_c=0$, $\xi_v=0.025$. The damping constants of SQZS-VI and Linear VI are set to be equal to the viscous friction constant of AQZS-VI, i.e., $c_s=c_l=c$. Therefore, it can be deduced that $\xi_s=\xi_l=\sqrt{\frac{k_{ref}}{k_l}}\xi_v=2.14\times0.025=0.0535$.

The comparison results are shown in **Fig. 21.** From the figure, it can be concluded that both AQZS-VI and SQZS-VI exhibit harden spring properties for which the transmissibility-frequency curves near resonant frequency bend to the right-hand sides.

The unbounded displacement transmissibility of SQZS-VI occurs at resonant frequency and AQZS-VI has lower peak value of displacement transmissibility than the SQZS-VI. The AQZS-VI is more stable than the SQZS-VI. The starting isolation frequency of AQZS-VI is lower than that of SQZS-VI and Linear VI. Under the same damping properties, the vibration isolation performance of AQZS-VI under displacement excitation is better than that of other two isolators with smaller starting frequency of isolation and stable performance.

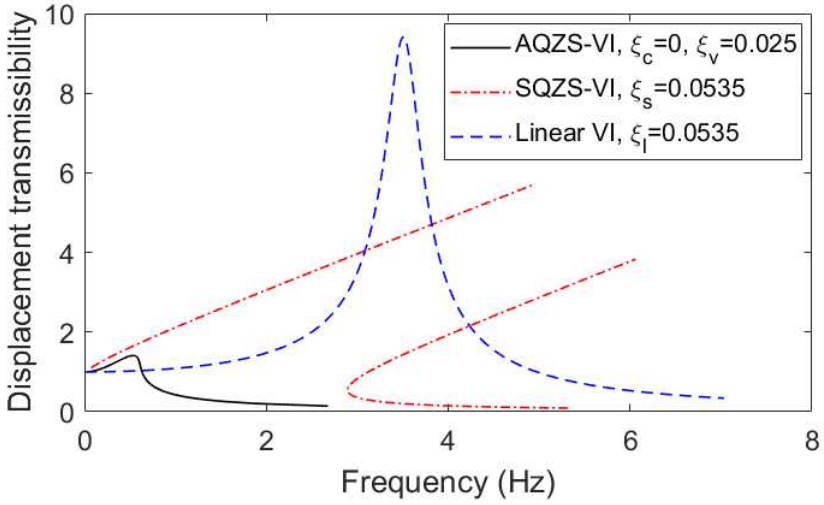


Fig. 21 Vibration isolation performance comparison of the three isolators under base displacement excitation ($z_0 = 0.1$).

7. Experimental investigation

7.1 Static experiments

The prototype of the proposed AQZS-VI was constructed to verify the accuracy of theoretical analysis. It is noted that the detailed structure of prototype will be introduced in next section. The static experimental setup is built and shown in Fig. 22 (a). The vertical lifting table combined with a force sensor is used to measure the force-displacement characteristics of the NSE, coil springs and the vibration isolator. The

743 supporting platform of prototype is fixed on the top fixed plate of the vertical lifting
744 table. The base plate of the prototype moves up and down under the thrust of the moving
745 plate of the vertical lifting table. The force sensor is placed between the base plate of
746 prototype and the moving plate of the vertical lifting table to measure the thrust applied
747 to the base plate of the prototype. The restoring force-displacement curves of the NSE,
748 and of the AQZS-VI with two coil springs (whose stiffness is k=0.92 $\mathrm{N\ mm^{-1}}$), and
749 of the AQZS-VI with two coil springs (whose stiffness is k=1.15 $\mathrm{N\ mm^{-1}}$) are shown
750 in Fig. 22 (c) (b) and (d) respectively.

751 From Fig. 22 (c), it can be obtained that the experimental result of the restoring
752 force-displacement curve of the NSE can basically fit the theoretical curve of the NSE,
753 which verifies the correctness of the static model. While the slope of the initial descent
754 section of the restoring force-displacement curve of the NSE is lower than that of the
755 theoretical curve, that is, the minimum dynamic stiffness of the NSE obtained from the
756 experiment is lower than that of the theoretical calculation. The reason for the difference
757 may be the approximation error during the modeling of the NSE as expressed in Eqs.
758 (10) and (11). The difference mentioned above leads to that the AQZS-VI composed of
759 the NSE and two springs with stiffness of k=0.92 $\mathrm{N\ mm^{-1}}$ exhibits negative stiffness
760 characteristic near the ZSP, as shown in Fig. 22 (b). It is worth noting that the stiffness
761 of two springs (k=0.92 $\mathrm{N\ mm^{-1}}$) is close to the theoretical required stiffness value for
762 AQZS-VI to achieve quasi-zero stiffness properties. Therefore, increasing the stiffness
763 of the two coil springs, that is, making k=1.15 $\mathrm{N\ mm^{-1}}$, can make the prototype
764 achieve quasi-zero stiffness characteristics near the ZSP, as shown in Fig. 22 (d). In
765 addition, observed from the experimental restoring force-displacement hysteresis
766 curves of the prototype, it can be concluded that the isolator has large damping
767 characteristics.

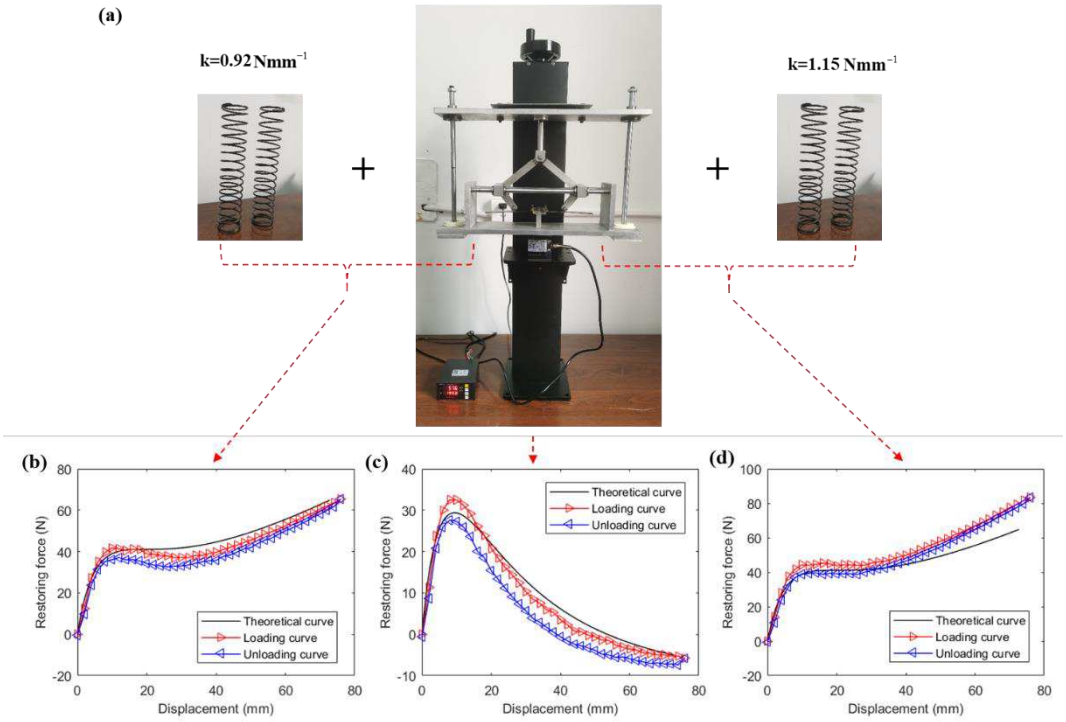


Fig. 22 (a) The static experimental setup of the prototype, and the restoring force-displacement curves (b) of the AQZS-VI with two coil springs (k=0.92 N mm^{-1}), (c) of the NSE and (d) of the AQZS-VI with two coil springs (k=1.15 N mm^{-1}).

7.2 Sinusoidal vibration excitation experiments

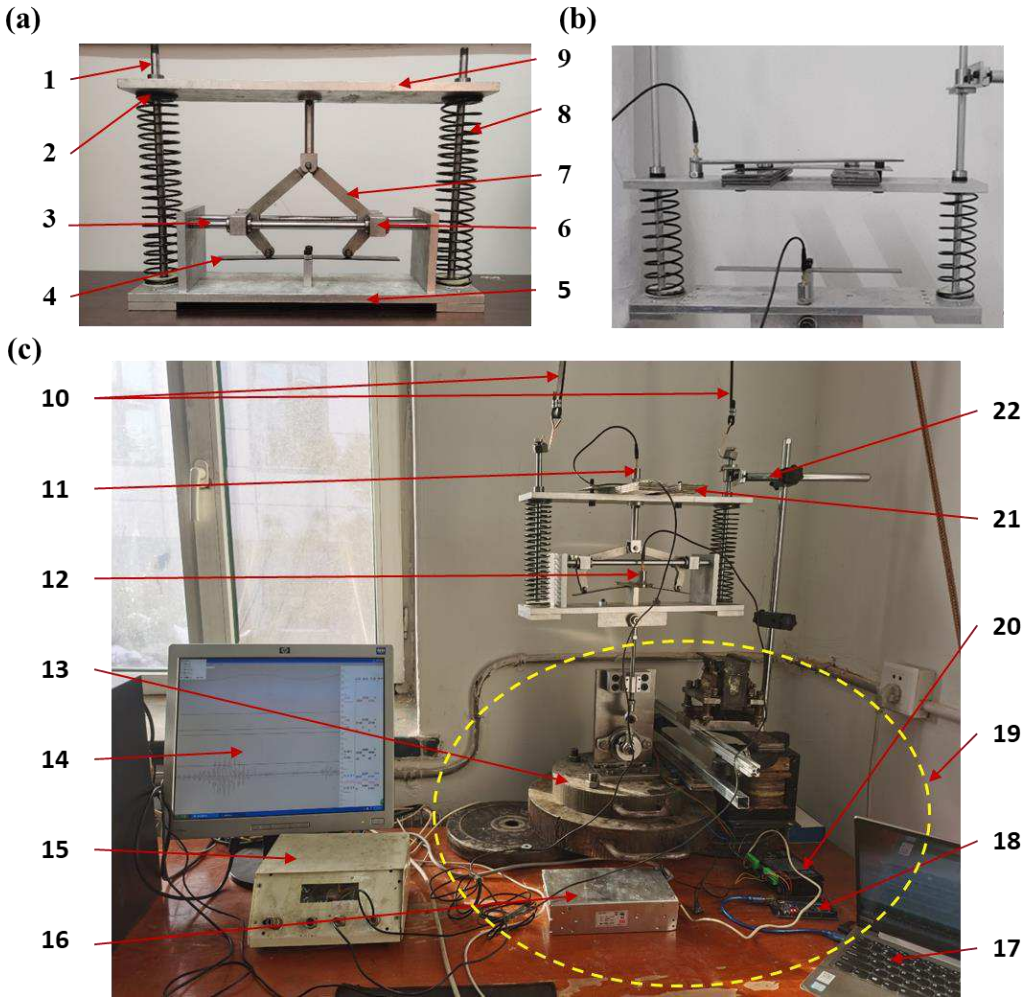
The prototype of the AQZS-VI and the linear vibration isolator (Linear VI) as well as the experimental setup are shown in Fig. 23 (a) (b) and (c) respectively. The length and height of the prototype are 420 mm and 310 mm, respectively. The main structural parameters of the prototype are shown in Table 1. There are no active or semi-active devices involved in the nonlinear isolator. To reduce the friction force of the prototype, several linear bearings and rolling bearings are used to transform the sliding friction into rolling friction, as shown in Fig. 23 (a). Specifically, two rolling bearings are installed at the end of L-shaped levers' short arm, and six linear bearings and four smooth shafts are used in vertical sliding pairs and horizontal sliding pairs to reduce friction. The spring stiffness of the Linear VI is 2 N mm^{-1}, which makes the Linear VI has the same bearing capacity with the AQZS-VI under specified deformation (20

784 mm).

785 **Table 1** The main structural parameters of the prototype

Structural parameters	Symbol	Value
Length of short arm of the L-shaped lever	l_1	50 mm
Length of long arm of the L-shaped lever	l_2	110 mm
Distance between un-deformed plate spring and horizontal guiding shaft	d	37.5 mm
Total stiffness of two vertical coil springs	k	1.15N mm^{-1}
Thickness of plate spring	h	1.5 mm
Width of plate spring	b	20 mm

786 As shown in Fig. 23 (c), a mechanical vibration exciter with a crank (eccentric
787 wheel) slider mechanism driven by a stepping motor is built to provide the displacement
788 excitation of the vibration isolator. The exciter can output harmonic vibration excitation
789 with the frequency changed from 0 Hz to 6 Hz, and the displacement amplitude of
790 vibration excitation can be adjusted from 0 mm to 10 mm. The base plate of the
791 prototype is connected with the exciting rod of the vibration exciter. The prototype is
792 suspended in the air by spring rope to offset its weight. Two piezoelectric
793 accelerometers (sensitivity: 500 mV/g) are fixed on the base and the supporting
794 platform respectively to detect their accelerations. The sampling frequency of data
795 acquisition device is 1000 Hz. The mass of foundation block (75 kg) is more than 10
796 times of the prototype mass of vibration isolator (5 kg), which can ensure the exciter
797 output ideal displacement excitation.



798

799 **Fig. 23** (a) The prototype of the AQZS-VI, (b) the linear vibration isolator and (c) the experimental
800 setup of vibration excitation. 1-Vertical guiding shaft, 2-Linear bearing, 3-Horizontal guiding shaft, 4-
801 Plate spring, 5-Base plate, 6-Horizontal guiding component, 7-L-shaped lever, 8-Coil spring, 9-
802 Supporting platform, 10-Suspension spring rope, 11-Accelerometer 2, 12-Accelerometer 1, 13-
803 Foundation block, 14-Data display interface, 15-Data acquisition device, 16-Power supply, 17-
804 Programming PC, 18-Controller, 19-Mechanical vibration exciter, 20-Motor driver, 21-Payload mass,
805 22-Vertical guiding component.

806 Sinusoidal vibration excitation of different frequencies from 1 Hz to 5.5 Hz is
807 applied to the base of the AQZS-VI prototype and of the Linear VI to analyze their
808 vibration isolation performance. The payload mass of the two isolators are all set to be
809 m=4.5 kg. The amplitude of displacement excitation is 5 mm which is equal to the non-

dimensional amplitude of displacement excitation used in theoretical analysis. The acceleration transmissibility defined as the ratio of the acceleration amplitude of the supporting platform to that of the base is used to evaluated the vibration isolation performance of the two isolators. Observed from the experimental results of linear vibration isolator, it can be seen that the acceleration transmissibility at resonance frequency is near 25. Therefore, the damping factor of linear vibration isolator can be calculated as $\xi_l = 0.02$ which is used to theoretical investigate the vibration transmissibility of the linear isolator. Similarly, it is reasonable to speculate that the viscous damping factor of the AQZS-VI prototype is $\xi_v = 0.02$. Therefore, in theoretical analysis, the damping parameters of the AQZS-VI are set to be $\xi_v = 0.02$, $\xi_c = 0.0001$, $\frac{f_{c2}}{f_{c1}} = 1$, $\frac{f_{c3}}{f_{c1}} = 2$ and $\frac{f_{c4}}{f_{c1}} = 2$.

The experimental results of discrete sinusoidal vibration excitation are compared with the theoretical analysis results as shown in Fig. 24. Observed from Fig. 24, the experimental results of the AQZS-VI and the linear vibration isolator are in good agreement with their theoretical analysis results. For the linear vibration isolator, the initial isolation frequency is higher than 5 Hz, which is much larger than the initial isolation frequency of AQZS-VI (1.2 Hz). For the AQZS-VI, the prototype performs rigid motion in low-frequency range, and the vibration isolation starts to take effect when the excitation frequency exceeds 1.2 Hz. No resonance phenomenon occurs along the whole vibration excitation frequency. From Figs. 19 and 24, it can be seen that large Coulomb friction force makes the resonance phenomenon disappear and be replaced by the rigid motion. And the Coulomb friction force also makes the vibration transmissibility-frequency curve shift to the right, increase the starting frequency of isolation and degrades the isolation performance. Therefore, reducing the Coulomb friction becomes the key factor of improving the vibration isolation performance of the AQZS-VI. Although the Coulomb friction damping deteriorates the vibration isolation performance of the prototype, the AQZS-VI also exhibits superior vibration isolation

performance compared with linear vibration isolator, and has great potential for engineering application.

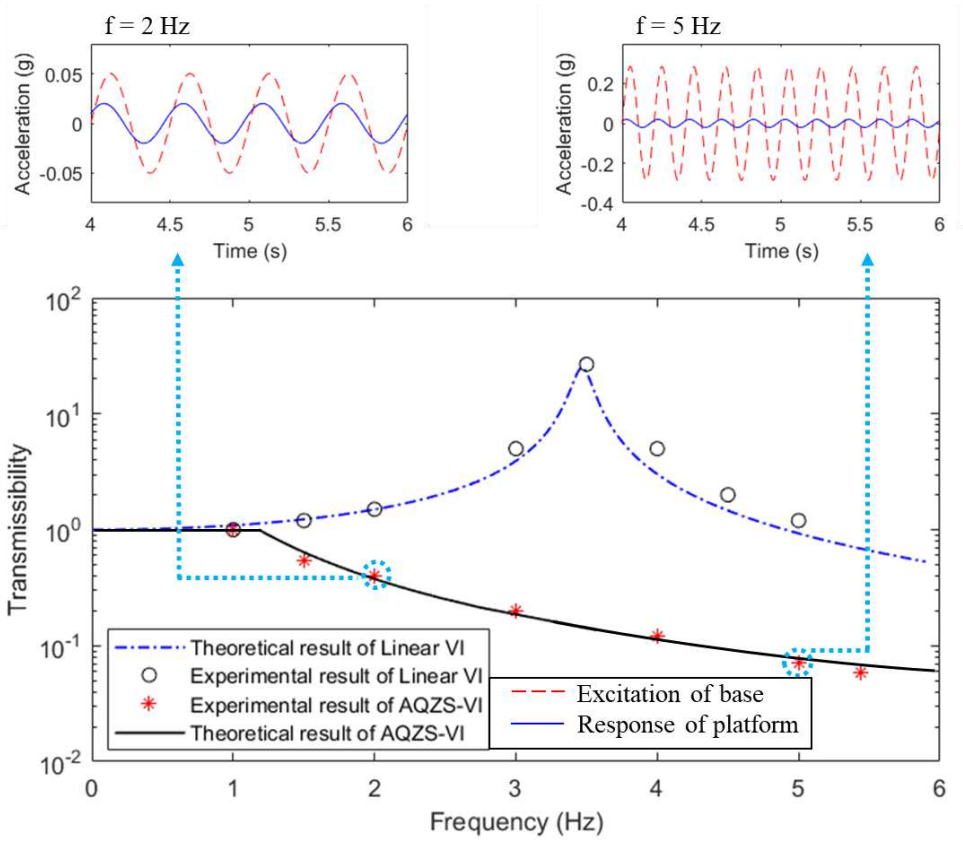


Fig. 24 Comparison of experimental and theoretical results: acceleration transmissibility of AQZS-VI and corresponding linear vibration isolator under sinusoidal displacement excitation with damping parameters $\xi_v = 0.02$, $\xi_c = 0.0001$, $\frac{f_{c2}}{f_{c1}} = 1$, $\frac{f_{c3}}{f_{c1}} = 2$, $\frac{f_{c4}}{f_{c1}} = 2$ and $\xi_l = 0.02$.

8. Conclusions and discussions

Taking advantage of the nonlinear benefits, a passive asymmetric quasi-zero stiffness vibration isolator (AQZS-VI) comprised of positive stiffness springs in parallel with negative stiffness element (NSE) is presented, of which the NSE is mainly constructed by the combination of cantilever plate spring and L-shaped lever (CPS-LSL). The static and dynamic models of the AQZS-VI are deduced considering the geometrical nonlinearity of the NSE. Base on the established model of the nonlinear

isolator, the static and dynamic properties of the AQZS-VI are thoroughly investigated. Comparing with traditional linear vibration isolator and the symmetric QZS-VI (SQZS-VI) comprising two oblique springs acting in parallel with one vertical spring, the AQZS-VI has superior asymmetric stiffness properties and exhibits excellent vibration isolation performance. Based on the results of this research, the following points can be obtained.

(a) Better than other QZS-VIs whose NSEs do not provide supporting force at zero stiffness point (ZSP), the NSE of the proposed AQZS-VI provides more supporting force than the parallel connected linear springs at ZSP, which is very beneficial for improving the bearing capacity of the isolator.

(b) The displacement range of AQZS-VI with low dynamic stiffness is much larger than that of SQZS-VI. With the same bearing capacity, the AQZS-VI has much longer working stroke than the SQZS-VI for low frequency vibration isolation.

(c) Under the same damping properties, the AQZS-VI can achieve smaller starting frequency of isolation, lower peak value of displacement transmissibility than the SQZS-VI and the traditional linear vibration isolator.

(d) The kinematic pairs of AQZS-VI increase the Coulomb friction force of the vibration isolator, which deteriorates its vibration isolation performance ---giving birth to rigid motion in the low frequency region, raising the starting frequency of vibration isolation and increasing the vibration transmissibility.

The AQZS-VI equipped with CPS-LSL possesses beneficial nonlinear stiffness properties, and provides a practical passive solution for achieving low and even ultra-low frequency vibration isolation. Much better vibration isolation performance and static bearing capacity can be achieved by using CPS-LSL in the vibration isolator. Further research should be devoted to improve the structural design and reduce the Coulomb friction of the isolator.

Acknowledgements

This work was supported by the National Key R&D Program of China (2016YFC0802900), the National Natural Science Foundation of China (51905210), the Jilin Province Key R&D Program of China (20200401130GX) and the Foundation for Innovative Research Groups of the National Natural Science Foundation of Hebei Province (E2020203174). The authors would like to thank all reviewers for their useful comments and suggestions to improve the quality of this paper.

Declarations

Conflicts of interest/Competing interests

The authors declare that they have no conflict of interest.

Availability of data and material

Data will be made available on reasonable request.

Appendix A

$$f_{f1} = 2f_{c1} \tag{A.1}$$

$$f_{f2} = 4\frac{\tilde{u}^2}{\delta^2-\tilde{u}^2} f_{c2} \tag{A.2}$$

$$f_{f3} = \frac{2}{\delta}\left(\cos\beta_c - \sin\beta_c \frac{\tilde{u}}{\sqrt{\delta^2-\tilde{u}^2}}\right) f_{c3} \tag{A.3}$$

$$f_{f4} = 2\frac{\delta^2}{\delta^2-\tilde{u}^2} f_{c4} \tag{A.4}$$

$$\varepsilon_0 = 4f_{c2} \frac{\tilde{u}^2}{\delta^2-\tilde{u}^2}\Big|_{\tilde{u}=\tilde{u}_0} \tag{A.5}$$

$$\varepsilon_1 = 8f_{c2} \frac{\delta^2\tilde{u}}{(\delta^2-\tilde{u}^2)^2}\Big|_{\tilde{u}=\tilde{u}_0} \tag{A.6}$$

$$\varepsilon_2 = 4f_{c2} \frac{\delta^4+3\delta^2\tilde{u}^2}{(\delta^2-\tilde{u}^2)^3}\Big|_{\tilde{u}=\tilde{u}_0} \tag{A.7}$$

$$\varepsilon_3 = 2f_{c3} \frac{1}{\delta}\left(\cos\beta_c - \sin\beta_c \frac{\tilde{u}}{\sqrt{\delta^2-\tilde{u}^2}}\right)\Big|_{\tilde{u}=\tilde{u}_0} \tag{A.8}$$

$$\varepsilon_4 = -2f_{c3} \frac{1}{\delta}\left[\left(\sin\beta_c + \cos\beta_c \frac{\tilde{u}}{\sqrt{\delta^2-\tilde{u}^2}}\right)\frac{d\beta_c}{d\tilde{u}} + \sin\beta_c\delta^2(\delta^2-\tilde{u}^2)^{-\frac{3}{2}}\right]\Big|_{\tilde{u}=\tilde{u}_0} \tag{A.9}$$

$$\varepsilon_5 = -f_{c3} \frac{1}{\delta}\left[\left(\cos\beta_c - \sin\beta_c \frac{\tilde{u}}{\Delta}\right)\left(\frac{d\beta_c}{d\tilde{u}}\right)^2 + 2\cos\beta_c\delta^2\Delta^{-3}\frac{d\beta_c}{d\tilde{u}} + \left(\sin\beta_c + \cos\beta_c\frac{\tilde{u}}{\Delta}\right)\frac{d^2\beta_c}{d\tilde{u}^2} + 3\sin\beta_c\delta^2\Delta^{-5}\tilde{u}\right]\Big|_{\tilde{u}=\tilde{u}_0} \tag{A.10}$$

Where $\Delta = \sqrt{\delta^2-\tilde{u}^2}$.

$$\varepsilon_6 = 2f_{c4} \frac{\delta^2}{\delta^2-\tilde{u}^2}\Big|_{\tilde{u}=\tilde{u}_0} \tag{A.11}$$

$$\varepsilon_7 = 4f_{c4} \frac{\delta^2\tilde{u}}{(\delta^2-\tilde{u}^2)^2}\Big|_{\tilde{u}=\tilde{u}_0} \tag{A.12}$$

$$\varepsilon_8 = 2f_{c4} \frac{\delta^4+3\delta^2\tilde{u}^2}{(\delta^2-\tilde{u}^2)^3}\Big|_{\tilde{u}=\tilde{u}_0} \tag{A.13}$$

Appendix B

The equations for a, a_0 and φ obtained by applying HBM are listed as below.

$$\left[\frac{8}{\pi}\xi_c\left(\mu_{10}+\mu_{11}a_0+\mu_{12}{a_0}^2+\frac{1}{3}\mu_{12}\mathrm{a}^2\right)+2\mathrm{a}\Omega\xi_v\right]\sin\varphi-[\Big(\varphi_1+2\varphi_2a_0+3\varphi_3{a_0}^2+4\varphi_4{a_0}^3+5\varphi_5{a_0}^4)\,\mathrm{a}+\frac{3}{4}(\varphi_3+4\varphi_4a_0+10\varphi_5{a_0}^2)\mathrm{a}^3+\frac{5}{8}\varphi_5\mathrm{a}^5-\mathrm{a}\Omega^2\Big]\cos\varphi+\Omega^2z_0=0 \tag{B. 1}$$

$$\left[\frac{8}{\pi}\xi_c\left(\mu_{10}+\mu_{11}\mathrm{a}_0+\mu_{12}{\mathrm{a}_0}^2+\frac{1}{3}\mu_{12}\mathrm{a}^2\right)+2\mathrm{a}\Omega\xi_v\right]\cos\varphi+[(\varphi_1+2\varphi_2a_0+3\varphi_3{a_0}^2+4\varphi_4{a_0}^3+5\varphi_5{a_0}^4)\,a+\frac{3}{4}(\varphi_3+4\varphi_4a_0+10\varphi_5{a_0}^2)\mathrm{a}^3+\frac{5}{8}\varphi_5\mathrm{a}^5-\mathrm{a}\Omega^2]\sin\varphi=0 \tag{B. 2}$$

$$\varphi_1a_0+\varphi_2{a_0}^2+\varphi_3{a_0}^3+\varphi_4{a_0}^4+\varphi_5{a_0}^5+\frac{1}{2}(\varphi_2+3\varphi_3a_0+6\varphi_4{a_0}^2+10\varphi_5{a_0}^3)a^2+\frac{3}{8}(\varphi_4+5\varphi_5a_0)a^4=0 \tag{B. 3}$$

References

1. J. Kim, Y. Jeon, S. Um, U. Park, K.-S. Kim, S. Kim, A Novel Passive Quasi-Zero Stiffness Isolator for Ultra-Precision Measurement Systems, Int. J. Precis. Eng. Man. 20, 1573-1580 (2019). https://doi.org/10.1007/s12541-019-00149-2

2. J.Z. Zhang, D. Li, M.J. Chen, S. Dong, An Ultra-Low Frequency Parallel Connection Nonlinear Isolator for Precision Instruments, Key Eng. Mater. 257-258, 231-238 (2004). https://doi.org/DOI 10.4028/www.scientific.net/KEM.257-258.231

3. T.D. Le, K.K. Ahn, A vibration isolation system in low frequency excitation region using negative stiffness structure for vehicle seat, J. Sound Vib. 330, 6311-6335 (2011). https://doi.org/10.1016/j.jsv.2011.07.039

4. T.D. Le, K.K. Ahn, Experimental investigation of a vibration isolation system using negative stiffness structure, Int. J. Mech. Sci. 70, 99-112 (2013). https://doi.org/10.1016/j.ijmecsci.2013.02.009

5. A.O. Oyelade, Vibration isolation using a bar and an Euler beam as negative stiffness for vehicle seat comfort, Adv. Mech. Eng. 11 (2019). https://doi.org/Artn 168781401986098310.1177/1687814019860983

6. H. Dai, X. Jing, Y. Wang, X. Yue, J. Yuan, Post-capture vibration suppression of spacecraft via a bio-inspired isolation system, Mech. Syst. Signal Process. 105, 214-240 (2018). https://doi.org/10.1016/j.ymssp.2017.12.015

7. Y.-S. Lin, R.W.K. Chan, H. Tagawa, Earthquake early warning-enabled smart base isolation system, Automat. Constr. 115 (2020). https://doi.org/10.1016/j.autcon.2020.103203

8. M. D'Amato, R. Laguardia, R. Gigliotti, Seismic Retrofit of an Existing RC Building With Isolation Devices Applied at Base, Frontiers in Built Environment, 6 (2020). https://doi.org/10.3389/fbuil.2020.00082

9. R.A. Ibrahim, Recent advances in nonlinear passive vibration isolators, J. Sound Vib. 314, 371-452 (2008). https://doi.org/10.1016/j.jsv.2008.01.014

10. C. Liu, X. Jing, S. Daley, F. Li, Recent advances in micro-vibration isolation, Mech. Syst. Signal Process. 56-57, 55-80 (2015). https://doi.org/10.1016/j.ymssp.2014.10.007

11. S.S. Rao, Mechanical vibrations, Pearson Education Inc, New York, 2010.

12. A. Carrella, M.J. Brennan, T.P. Waters, Static analysis of a passive vibration isolator with quasi-zero-stiffness characteristic, J. Sound Vib. 301, 678-689 (2007). https://doi.org/10.1016/j.jsv.2006.10.011

13. I. Kovacic, M.J. Brennan, T.P. Waters, A study of a nonlinear vibration isolator with

a quasi-zero stiffness characteristic, J. Sound Vib. 315, 700-711 (2008). https://doi.org/10.1016/j.jsv.2007.12.019

14. Z. Hu, X. Wang, H. Yao, G. Wang, G. Zheng, Theoretical Analysis and Experimental Identification of a Vibration Isolator With Widely-Variable Stiffness, J. Vib. Acoust. 140 (2018). https://doi.org/10.1115/1.4039537

15. J. Zhou, X. Wang, D. Xu, S. Bishop, Nonlinear dynamic characteristics of a quasi-zero stiffness vibration isolator with cam–roller–spring mechanisms, J. Sound Vib. 346, 53-69 (2015). https://doi.org/10.1016/j.jsv.2015.02.005

16. Y. Liu, L. Xu, C. Song, H. Gu, W. Ji, Dynamic characteristics of a quasi-zero stifness vibration isolator with nonlinear stiffness and damping, Arch. Appl. Mech. 89, 1743-1759 (2019). https://doi.org/10.1007/s00419-019-01541-0

17. N. Zhou, K. Liu, A tunable high-static–low-dynamic stiffness vibration isolator, J. Sound Vib. 329, 1254-1273 (2010). https://doi.org/10.1016/j.jsv.2009.11.001

18. X. Liu, X. Huang, H. Hua, On the characteristics of a quasi-zero stiffness isolator using Euler buckled beam as negative stiffness corrector, J. Sound Vib. 332, 3359-3376 (2013). https://doi.org/10.1016/j.jsv.2012.10.037

19. D. Xu, Q. Yu, J. Zhou, S.R. Bishop, Theoretical and experimental analyses of a nonlinear magnetic vibration isolator with quasi-zero-stiffness characteristic, J. Sound Vib. 332, 3377-3389 (2013). https://doi.org/10.1016/j.jsv.2013.01.034

20. W. Wu, X. Chen, Y. Shan, Analysis and experiment of a vibration isolator using a novel magnetic spring with negative stiffness, J. Sound Vib. 333, 2958-2970 (2014). https://doi.org/10.1016/j.jsv.2014.02.009

21. X. Huang, X. Liu, J. Sun, Z. Zhang, H. Hua, Vibration isolation characteristics of a nonlinear isolator using Euler buckled beam as negative stiffness corrector: A theoretical and experimental study, J. Sound Vib. 333, 1132-1148 (2014). https://doi.org/10.1016/j.jsv.2013.10.026

22. B.A. Fulcher, D.W. Shahan, M.R. Haberman, C. Conner Seepersad, P.S. Wilson, Analytical and Experimental Investigation of Buckled Beams as Negative Stiffness Elements for Passive Vibration and Shock Isolation Systems, J. Vib. Acoust. 136 (2014). https://doi.org/Artn 03100910.1115/1.4026888

23. X. Sun, X. Jing, J. Xu, L. Cheng, Vibration isolation via a scissor-like structured platform, J. Sound Vib. 333, 2404-2420 (2014). https://doi.org/10.1016/j.jsv.2013.12.025

24. X. Sun, X. Jing, Analysis and design of a nonlinear stiffness and damping system with a scissor-like structure, Mech. Syst. Signal Process. 66-67, 723-742 (2016). https://doi.org/10.1016/j.ymssp.2015.05.026

25. X. Jing, L. Zhang, X. Feng, B. Sun, Q. Li, A novel bio-inspired anti-vibration

structure for operating hand-held jackhammers, Mech. Syst. Signal Process. 118, 317-339 (2019). https://doi.org/10.1016/j.ymssp.2018.09.004

26. C. Liu, X. Jing, F. Li, Vibration isolation using a hybrid lever-type isolation system with an X-shape supporting structure, Int. J. Mech. Sci. 98, 169-177 (2015). https://doi.org/10.1016/j.ijmecsci.2015.04.012

27. X. Sun, X. Jing, A nonlinear vibration isolator achieving high-static-low-dynamic stiffness and tunable anti-resonance frequency band, Mech. Syst. Signal Process. 80, 166-188 (2016). https://doi.org/10.1016/j.ymssp.2016.04.011

28. C. Liu, X. Jing, Z. Chen, Band stop vibration suppression using a passive X-shape structured lever-type isolation system, Mech. Syst. Signal Process. 68-69, 342-353 (2016). https://doi.org/10.1016/j.ymssp.2015.07.018

29. J. Bian, X. Jing, Superior nonlinear passive damping characteristics of the bio-inspired limb-like or X-shaped structure, Mech. Syst. Signal Process. 125, 21-51 (2019). https://doi.org/10.1016/j.ymssp.2018.02.014

30. G. Yan, H. Zou, S. Wang, L. Zhao, Q. Gao, T. Tan, W. Zhang, Large stroke quasi-zero stiffness vibration isolator using three-link mechanism, J. Sound Vib. 478 (2020).

31. X. Zhou, X. Sun, D. Zhao, X. Yang, K. Tang, The Design and Analysis of a Novel Passive Quasi-Zero Stiffness Vibration Isolator, J. Vib. Eng. Technol. 9, 225–245 (2021). https://doi.org/10.1007/s42417-020-00221-6

32. T. Belendez, C. Neipp, A. Belendez, Large and small defections of a cantilever beam, Eur. J. Phys. 23 (2002) 371–379.

33. L. Chen, An integral approach for large deflection cantilever beams, Int. J. Nonlin. Mech. 45, 301-305 (2010). https://doi.org/10.1016/j.ijnonlinmec.2009.12.004

34. B.S. Shvartsman, Large deflections of a cantilever beam subjected to a follower force, J. Sound Vib. 304, 969-973 (2007). https://doi.org/10.1016/j.jsv.2007.03.010

35. C. Cheng, S. Li, Y. Wang, X. Jiang, Force and displacement transmissibility of a quasi-zero stiffness vibration isolator with geometric nonlinear damping, Nonlinear Dynam. 87, 2267-2279 (2016). https://doi.org/10.1007/s11071-016-3188-0

36. Z. Xiao, X. Jing, L. Cheng, The transmissibility of vibration isolators with cubic nonlinear damping under both force and base excitations, J. Sound Vib. 332, 1335-1354 (2013). https://doi.org/10.1016/j.jsv.2012.11.001

37. A.H. Nayfeh, D.T. Mook, Nonlinear Oscillations, Wiley-Interscience, New York, NY, 1979.